Defence Research and Development Canada
Recherche et développement pour la défense Canada

DRDC | RDDC

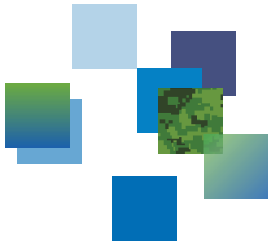

Validation of new crack monitoring technique for Victoria class high-pressure air bottles

Ian Thompson
John R. MacKay

Defence Research and Development Canada

Scientific Report
DRDC-RDDC-2014-R81
June 2014

Canada

Validation of new crack monitoring technique for Victoria class high-pressure air bottles

Ian Thompson
John R. MacKay

Defence Research and Development Canada
Scientific Report
DRDC-RDDC-2014-R81
June 2014

Abstract

High-pressure air bottles are used in the Victoria class submarines to supply breathing air and to provide pressurized air for surfacing. The bottles are exposed to cyclic loading, which may result in the initiation and growth of fatigue cracks. An internal crack-like indication in a high-pressure air bottle instigated this study to better understand the growth of potential fatigue cracks. This will enable better management of the remaining operating life of high-pressure air bottles with detected cracks.

In this study, the feasibility of using externally-mounted strain gauges to monitor the growth of known internal cracks in high-pressure air bottles was examined. A combination of numerical modelling and experiments was used to validate this technique. Two experimental samples were internally pressurized and external strain was measured. Reasonable agreement of measured strain with finite element analyses of the samples suggests the high-pressure air bottle finite element analyses results are reliable. Finite element analyses and experiments showed an area on the exterior of test samples opposite an internal notch with a modified strain field. The numerical analyses indicated that changes in the strain field associated with crack growth may be detected using external strain gauges. These results are consistent with a previous numerical analysis of a high-pressure air bottle which indicated the growth of internal cracks can be monitored with external strain gauges.

Digital image correlation was used to measure the strain field in the area opposite the internal notch. It was useful for identifying the precise location of the notch, but further improvements to its use are necessary to ensure reliable results. It shows promise as a method to identify the location of high-pressure air bottle internal cracks and to complement other non-destructive examination techniques.

Significance for defence and security

The crack monitoring technique that has been validated in this report may allow damaged high-pressure air bottles to remain in service for a limited time, thus increasing the availability of Victoria class submarines while replacement bottles are procured.

Résumé

Des bouteilles d'air à haute pression sont utilisées dans les sous-marins de classe Victoria afin d'assurer l'alimentation en air respirable et fournir l'air sous pression nécessaire lors de l'émersion. Ces bouteilles sont soumises à des charges cycliques pouvant provoquer l'apparition et favoriser la croissance de fissures de fatigue. L'observation d'une marque interne semblable à une fissure, dans une bouteille d'air à haute pression, est à l'origine de la mise en œuvre de la présente étude dont l'objectif est de mieux comprendre la croissance d'éventuelles fissures de fatigue. Les résultats permettront d'assurer une gestion plus efficace des bouteilles d'air à haute pression présentant des fissures durant le reste de leur durée de vie utile.

Dans le cadre de la présente étude, on a évalué la faisabilité d'utiliser des extensomètres externes pour surveiller la croissance des fissures internes détectées dans les bouteilles de ce type. La combinaison de résultats de modélisation numérique et d'expériences a servi à valider la technique employée. Deux échantillons expérimentaux ont été mis sous pression et la déformation externe a été mesurée. Il existe une concordance entre la déformation mesurée et les résultats de l'analyse par éléments finis des échantillons, ce qui laisse croire que ceux des bouteilles d'air à haute pression sont fiables. Les résultats de l'analyse par éléments finis et ceux des expériences indiquent qu'il y a modification du champ de déformation dans une zone située à l'extérieur des échantillons d'essai, du côté opposé à une entaille interne. Les résultats des analyses numériques indiquent que l'utilisation d'extensomètres externes pourrait permettre de détecter des variations du champ de déformation associées à la croissance de fissures.

Ces résultats concordent avec ceux d'une analyse numérique antérieure effectuée sur une bouteille d'air à haute pression, lesquels indiquaient que des extensomètres externes peuvent servir à surveiller la croissance de fissures internes. La technique de corrélation d'images numériques a été employée pour mesurer le champ de déformation dans la zone située du côté opposé à l'entaille interne. La technique est utile pour déterminer l'emplacement exact de l'entaille, mais il faudra améliorer certains paramètres d'utilisation pour garantir l'obtention de résultats fiables. La méthode semble toutefois prometteuse pour déterminer l'emplacement de fissures internes dans les bouteilles d'air à haute pression et comme complément aux autres techniques d'essais non destructifs.

Importance pour la défense et la sécurité

Les résultats des expériences décrites dans le présent rapport ont permis de valider une technique de surveillance de la croissance de fissures, laquelle pourrait permettre l'utilisation de bouteilles d'air à haute pression endommagées pendant une période restreinte, ce qui accroîtrait du même coup la disponibilité des sous-marins de classe Victoria pendant le processus d'acquisition de bouteilles de remplacement.

This page intentionally left blank.

Table of contents

List of figures

List of tables

Acknowledgements

The authors would like to thank colleagues at Dockyard Laboratory (Atlantic) for their assistance with this work. Tomasz Lemczyk conducted mechanical tests, Vincent Drover conducted chemical composition tests, and Paul Hamilton conducted non-destructive tests and provided valuable input on non-destructive testing.

This page intentionally left blank.

1 Introduction

High-pressure (HP) air bottles are used in the Victoria class submarines for emergency air and displacing water in the ballast tanks during surfacing. The vital nature of these activities means that the integrity of HP air bottles is critical to safe operation. As such, measures must be taken to ensure fracture or leakage is avoided. Currently, the bottles are periodically inspected and damaged bottles are removed from service.

In 2006, a crack-like indication was found on an air bottle during a routine eddy current inspection by Naval Engineering Test Establishment (NETE) [1]. The possibility of the presence of a crack in one of the bottles suggested that cracks may be present in other bottles. The long lead time required for delivery of new bottles motivated a study to better understand the growth of cracks in HP air bottles to determine if bottles with limited flaws could be left in service.

Dockyard Laboratory (Atlantic) was tasked to examine the crack-like indication, perform material testing, and conduct a fatigue assessment of the HP air bottles by DNPS 4-3-7 under the Submarine Scientific Support Service Level Agreement. BMT Fleet Technology was contracted by DRDC – Atlantic Research Centre to perform fatigue calculations and finite element analyses. The finite element analyses were conducted to determine the change in external strain in the vicinity of a crack. This was done to determine if externally mounted strain gauges are suitable to detect the growth of internal HP air bottle cracks.

This document covers the validation of the use of externally mounted strain gauges to monitor further growth of cracks of a limited size. Finite element analyses of experimental samples similar to air bottles were conducted using the same modelling techniques used by BMT Fleet Technology [2]. The results of the finite element analyses were compared to experimental results. Digital image correlation (DIC) was used in the experiments and its use, associated challenges, and potential future uses are discussed.

2 Background

2.1 Overview of high-pressure air bottles

The potentially catastrophic nature of a high-pressure air bottle failure has resulted in the development of standards to govern their manufacture and maintenance [3–5]. The damage mechanisms of most concern are pitting corrosion and corrosion fatigue [6]. The combination of pitting corrosion and corrosion fatigue may result in the introduction and growth of fatigue cracks due to the cyclic nature of the internal pressure load on the bottles. Air dryers are in place to reduce the humidity, but they are not sufficient to prevent corrosion.

Steel seamless HP air bottles are used in Victoria class submarines. They are made by Chesterfield Special Cylinders in the United Kingdom.

The pressure in the bottles is cycled, so the initiation and growth of fatigue cracks is a possibility, particularly in the presence of corrosion pits. The bottles are in several banks of bottles connected in series. A crack leading to bursting or leaking of a bottle could result in the loss of the contents of an entire bank of bottles. This could compromise the ability of a submarine to surface or could result in loss of emergency air.

Defence Standard 02-318 Parts 1 and 2 [4, 5] outline the required cleaning, inspection, and testing for high-pressure gas cylinders. Periodic visual inspection is required to identify damage, ultrasonic inspection is required over the surface to verify wall thickness, and hydrostatic proof testing is required to ensure adequate strength. Deviations are accepted from this procedure to allow onboard inspections provided proper permission is granted. For the Victoria class submarines, NETE performs visual inspections, eddy current inspections, and ultrasonic inspections every ten years. The eddy current and ultrasound inspection are conducted internally. The ultrasonic inspections consist of longitudinal ultrasound to determine the bottle's thickness and shear wave ultrasound to identify subsurface flaws. The eddy current inspection is conducted to detect internal surface flaws [7]. The inspection techniques used by NETE were developed based on similar techniques used by the Royal Navy [8].

2.2 Previous work

BMT Fleet Technology and DRDC performed a fatigue assessment, including determination of the critical crack size for the air bottles, performed additional inspections on the damaged bottle, and investigated potential crack monitoring techniques. The fatigue assessment performed by BMT Fleet Technology used methodologies specified by British Standard 7910 Level 2. The analyses indicated that an initially 2 mm deep, 10 mm long longitudinal crack could be cycled twice daily for approximately eight years before growing to a critical size [2]. This crack size was selected as these were the dimensions of the crack-like indication measured by NETE.

The crack-like indication in the air bottle was examined at Dockyard Laboratory (Atlantic) using several non-destructive techniques. Conventional and digital radiography, eddy current testing, ultrasonic testing, magnetic particle inspection, and visual inspection were performed on the sample. Lack of availability of identical eddy current probes, equipment, and standards prevented the inspections from being identical to that conducted by NETE. No defect indications were found, suggesting the indication may have been a false positive [9]. In discussions with NETE personnel, it was mentioned that the indication occurred consistently with the same eddy current equipment settings. They suggested a false positive could occur if the equipment was set to detect very small cracks, as was the case in this situation.

As reported in Reference 2, finite element analysis was used by BMT Fleet Technology to determine the strains present in a pressurized bottle with an internal longitudinally-oriented crack. External strains were determined for six crack sizes, an initially 2 mm deep, 10 mm long crack and cracks whose sizes were determined in a fatigue assessment following 1000, 3000, 5000, 6000, and 7000 load cycles. The analyzed crack sizes are shown in Table 1.

Table 1: *Sizes of internal cracks analyzed.*

Crack Size	Number of Pressure Cycles (at 30 MPa)	Crack Size Parameters (mm)	
		Crack Depth, a	Crack Length, $2c$
1	1	2.001	10.001
2	1000	3.173	11.657
3	3000	6.172	16.930
4	5000	10.199	25.200
5	6000	12.756	30.916
6	7000	15.893	38.384

The nominal wall thickness was used in the models with cracks. This results in lower external variations in strain than would occur with a reduced wall thickness for a given crack depth. The nominal wall thickness was used as this would result in lower external variations in strain than with a thinner wall for a given crack depth. The thickness of the bottle in the area of the neck where the thickness is not prescribed was determined by using a best-fit curve between areas of known dimensions. The model was meshed using ANSYS v.11 using SOLID185 elements. These are linear brick elements with eight nodes which each have three translational degrees of freedom.

The model was created as one quarter of the bottle due to the symmetry of the bottle and its loads. Constraints were applied on nodes through the wall thickness at the normal planes (centreline and mid-span) to provide continuity associated with the symmetric boundary conditions. Nodal constraints were removed with nodes associated with the crack size. Ten elements were used through the wall thickness. A solid cap was used at the flange neck. The material properties that were used in the model were the minimum specified yield strength of 700 MPa, modulus of elasticity of 206 GPa, density of 7850 kg/m^3, and Poisson's ratio of 0.287. The model is shown in Figure 1.

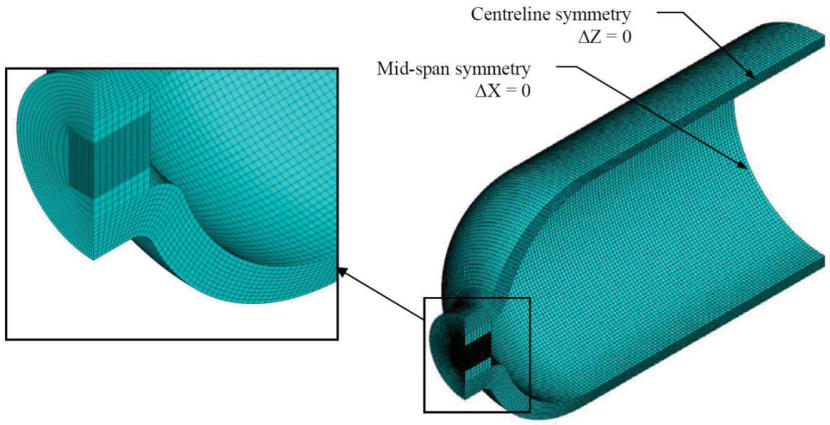

Figure 1: *Finite element model of HP air bottle created by BMT Fleet Technology.*

The model indicated that internal pressure causes the crack to open, resulting in local bending that reduces the strain on the external surface of the bottle immediately opposite the crack. As the crack grows larger, the calculated strain in this area decreases further. The calculated strain immediately opposite the crack was 304 $\mu\epsilon$ lower then the uncracked portion (1192 $\mu\epsilon$) for the initial crack and 553 $\mu\epsilon$ lower for the crack following 7000 load cycles. Localized flattening of the air bottle due to the presence of an internal crack also results in higher strains approximately 8 mm from the crack circumferentially. These strains increase as the internal crack grows. The differences in strain associated with the smallest and largest cracks analyzed compared to an uncracked bottle are shown in Figures 2 and 3, respectively.

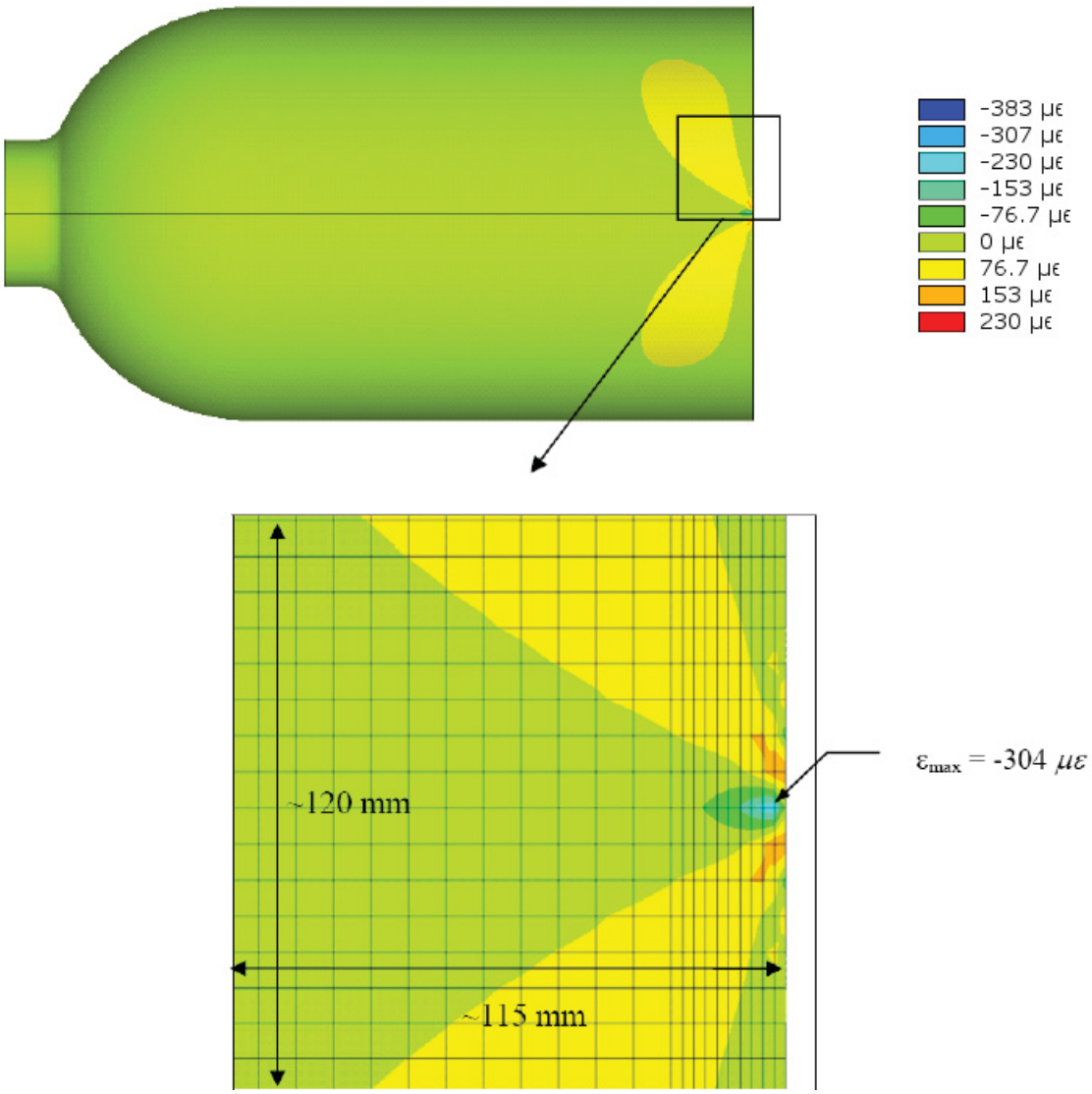

Figure 2: *Calculated change in circumferential strains for a HP air cylinder with a 2 mm deep, 10 mm long crack. [2]*

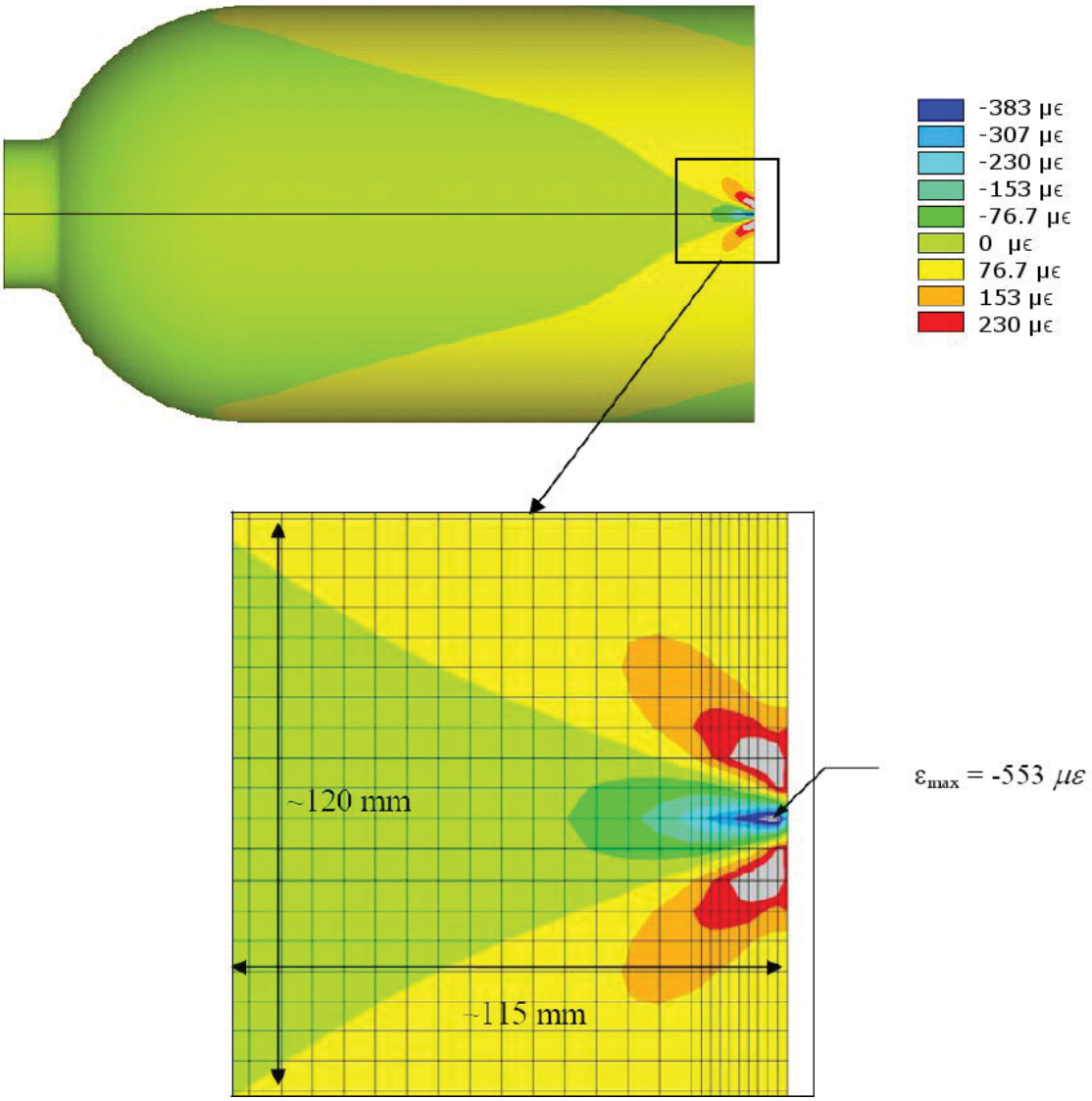

Figure 3: *Calculated change in circumferential strains for a HP air cylinder with a 16 mm deep, 38 mm long crack. [2]*

3 Methodology

3.1 Experimental samples

Further corroboration of the calculated HP air bottle strain field in the presence of a crack was desired so experimental samples were tested to validate the numerical results. Two experimental samples were fabricated from a single length of 6 inch Schedule 80 pipe. The outside diameter was 84 mm and the wall thickness was 11.2 mm on average but varied between 10.6 and 12.0 mm. Flat plates (25 mm thick) were attached to the ends using fillet welds to create a small pressure vessel. Threaded holes were machined into one of the flat plates for each sample to allow pressurizing. The two pipe sections were 60 cm long and had machined internal notches to act as stress raisers similar to cracks. The notches were 2.5 mm deep and 40 mm long. The loading and ratio of the radius to wall thickness of the samples are similar to that of typical Victoria class submarine high-pressure air bottles. A sketch is shown in Figure 4. One of the experimental samples is shown in Figure 5; close-up views of the internal notch and strain gauges on the opposite side are shown in Figure 6.

The experimental samples and HP air bottles were made from different steels. The yield strength of the steels were not the same but the elastic modulus should be similar. As the loading in the experiments was low, yielding beyond the notch tip was not expected.

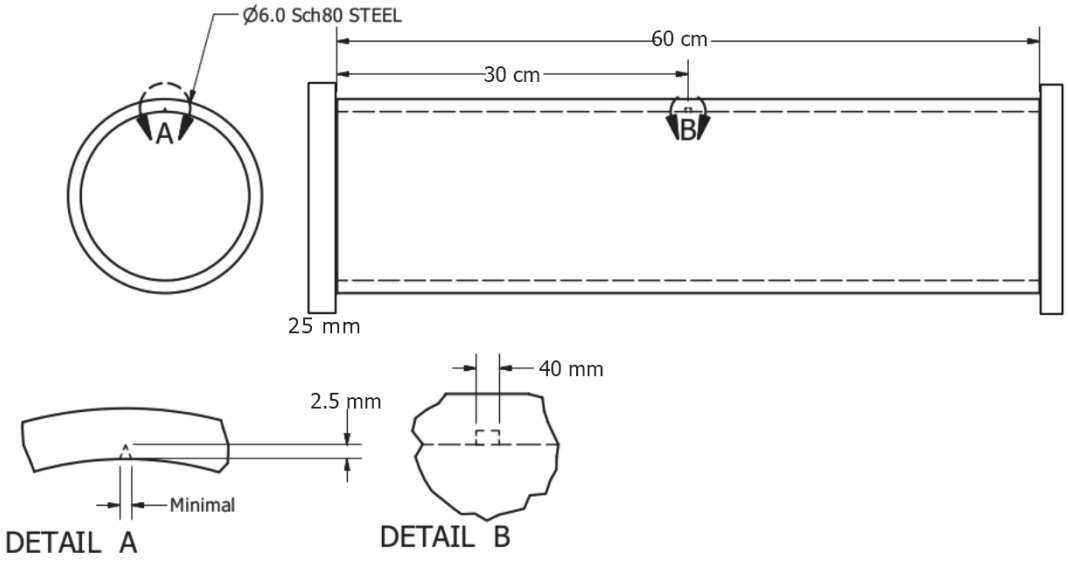

Figure 4: *Sketch of experimental sample.*

The outer surface of the cylinder in the vicinity of the notch was painted white with a speckling of black paint (as shown in Figure 5) to enable use of digital image correlation equipment, described further in the following section. Foil strain gauges were applied externally immediately opposite the notch and 90° away from the notch. The strain gauge 90° from the notch was intended to provide a comparison to measurements near the notch. Water pressure in the cylinders was increased with a pump and the pressure was measured using a digital pressure transducer.

Figure 5: *Experimental sample. Notch is located on interior surface at mid-height.*

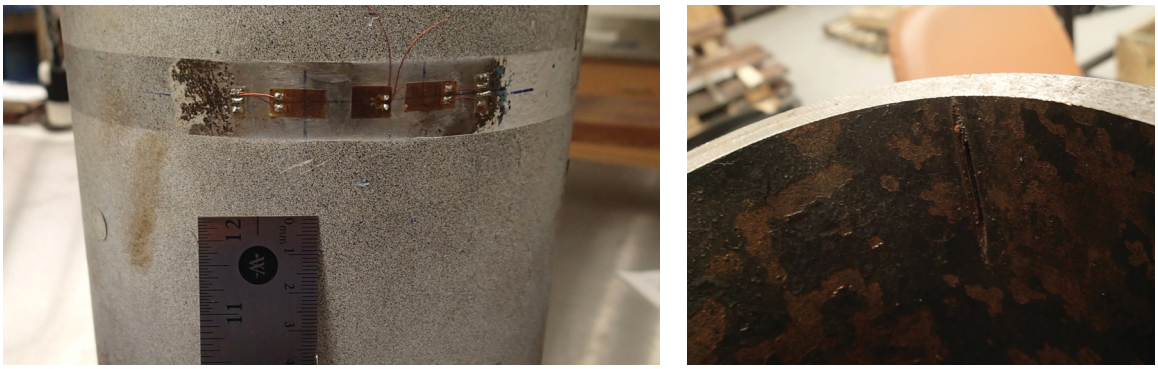

Figure 6: *Close-up views of external strain gauges (left) and internal notch shown after testing (right).*

3.2 Digital image correlation

Digital image correlation was used to measure the strain field on the external surface of the experimental sample. Digital image correlation provides a non-contact method to measure the strain and displacement fields for samples under load. Typically, samples without colour variation are painted with a black and white speckle pattern. The grey level of individual pixels on two digital images is compared to measure the deformation between images. A correlation function is used to compare the two images. Displacement vectors and their spatial derivatives are calculated that minimize the correlation coefficient [10]. This produces a continuous strain field, rather than the point measurements available from strain gauges. An example image taken using DIC is shown in Figure 7. In this image, the flange was pulled apart and the strain concentrations can be seen.

ARAMIS 3D 5M digital image correlation equipment with two 5 megapixel cameras using 50 mm Titanar lenses and ARAMIS version 6 software was used in these experiments. The use of two cameras recording at different angles enables differentiation between rigid body motion and strain. Prior to each experiment, the DIC equipment was calibrated using a CP 20/MV standard. The standard is shown to the right of the cylinder in Figure 8. Figure 9 shows the DIC cameras, lights, and tripod with the computer running the DIC software in the background.

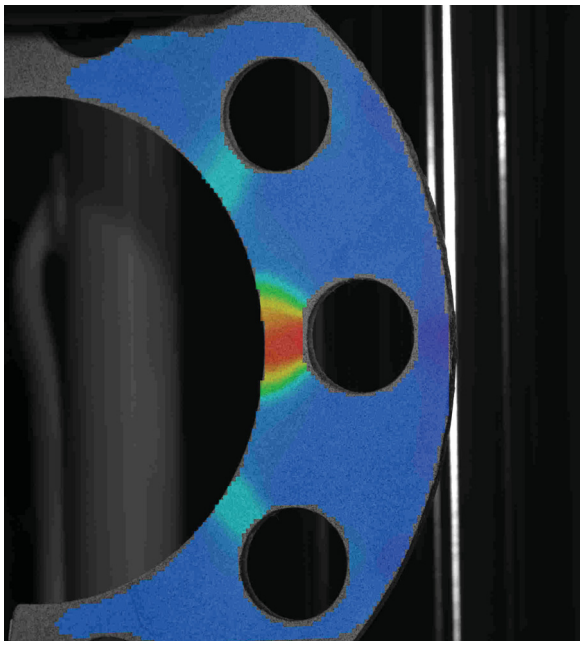

Figure 7: *Image taken using digital image correlation while flange is being pulled apart.*

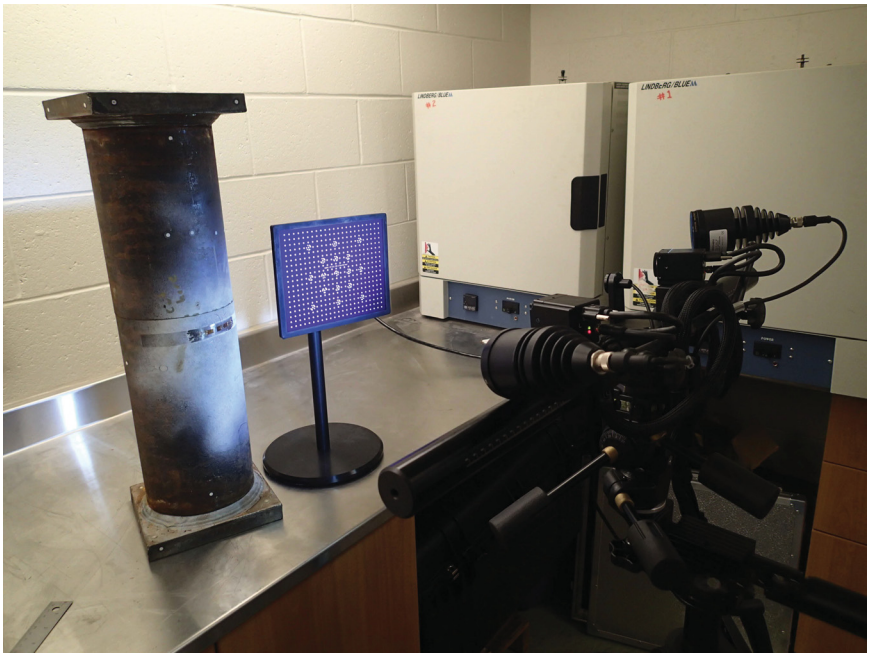

Figure 8: *Digital image correlation setup showing tripod with cameras, experimental sample, and calibration standard.*

Figure 9: *ARAMIS 3D 5M digital image correlation equipment. Lights and cameras are shown on the tripod and the computer running DIC software is shown in background.*

3.3 Notched cylinder finite element models

A finite element model of the cylinder with an internal notch was created to validate the results of the HP air bottle model with an internal crack and to provide further information on the strain field in the vicinity of a crack. Finite element simulation of the experiment, including model generation, analysis and post-processing, was performed using the ANSYS 14.0 commercial software. The finite element modelling methodology was based on the work reported in Reference 2 to the extent that was feasible.

The FE model of the test specimen is summarized in Figure 10, including the FE mesh, the geometry, and the assumed material properties. The dimensions of the model are based on average measured properties of the test specimens. All aspects of the test specimen, including the end cap, the pipe, and the end cap fillet weld, were modelled with 20 node continuum brick elements (SOLID186). These differ from the SOLID185 elements used in Reference 2 in that the SOLID186 elements have mid-side nodes. The pipe and end cap were assumed to be connected only through the fillet weld (i.e., the elements shown in orange in Figure 10). The target element size was 4 mm, except for the area in the vicinity of the notch, where a refined 1 mm mesh grid was used. Those targets resulted in four and twelve elements through the thickness of the pipe wall for the coarse and fine regions, respectively. Prismatic brick elements were used wherever possible; however, in certain areas, such as the transition region between the coarse and fine meshes, the "collapsed" 10 node tetrahedron version of the element was used. In total, there were 132,214 elements and 412,460 nodes in the model.

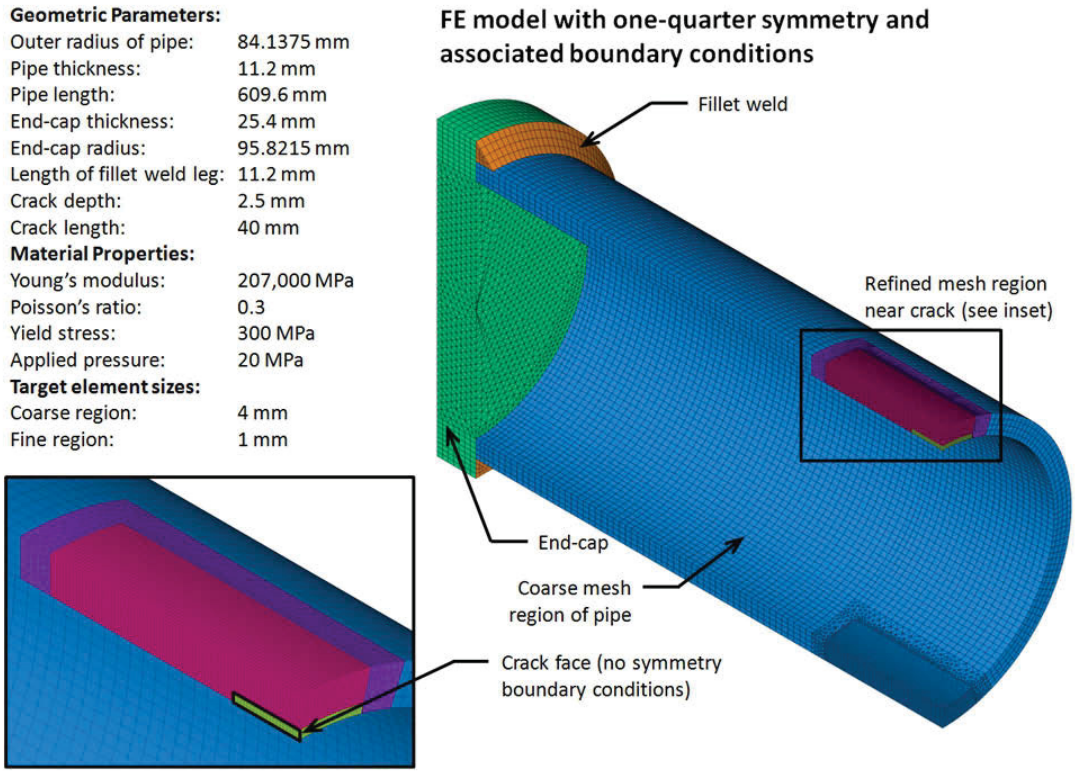

Figure 10: *Finite element model parameters and mesh configuration.*

Only one-quarter of the test specimen was modelled (one-half of the length and one-half of the circumference) in order to take advantage of symmetry. Symmetry was enforced by constraining the longitudinal displacement of nodes falling on the transverse symmetry plane and constraining the transverse displacement of nodes on the longitudinal plane of symmetry. The internal longitudinal notch was simulated by removing the symmetry constraints on the nodes associated with the face of the notch (see Figure 10). That allowed the notch to open under the internal pressure load, which was applied to the inside surface of the pipe and the end cap. One additional node on the end cap was constrained in the vertical direction in order to prevent rigid body motion. The response of the pipe was assumed to be linear-elastic for the current analysis.

In addition to the benchmark FE model described above, several other models were generated and analyzed. First, an additional refined FE model with approximately twice the number of elements and nodes (292,969 elements and 870,238 nodes) was produced in order to verify that the original mesh had converged sufficiently. In particular, the refined mesh had 16 elements through the pipe wall thickness in the crack region, compared to 12 in the benchmark model. The benchmark and refined models were identical in all respects other than the mesh size. Second, a series of models were generated to study how the strain response of the pipe might vary with the depth of the notch. Those models were identical to the original benchmark model in all respects except the notch depth (i.e., the material properties, overall geometry, crack length and mesh density were the same for all of the models).

4 Results and discussion

4.1 Experimental results

Two cylindrical samples with internal notches were internally pressurized and the resulting external strains were measured with foil strain gauges and digital image correlation. The test specimens are described further in Section 3.1.

4.1.1 Initial experiment

The initial experiment was run using strain gauges and digital image correlation to measure the strain on Sample 1 while under an internal pressure of 19 MPa. The point measurements from the strain gauges were intended to validate the DIC results and FE model. The DIC results were intended for comparison of the measured strain field with that calculated using finite element analysis.

DIC measurements were taken in an area centered approximately 25 mm below the strain gauges, which were intended to be located at the center of the notch. Circumferential strain results from consecutive DIC images are shown in Figures 11 and 12. The colours in the center area (area A in Figure 11) correspond to the strain legend on the right side of the figures (B). The line that runs across the plot (C) acts as a continuous virtual strain gauge. The strain values from the line are plotted in the middle of the figure (D). The plot on the right side of the graphic (E) is a histogram showing the distribution of pixels with different calculated strain values. The histogram provides an indication of the average and variance of the measured strain.

Both DIC images (Figures 11 and 12) show average circumferential strain values of approximately 450 $\mu\epsilon$ along the plotted line. The histogram in both figures show a similar average value of strain over each image but the variance is much larger in Figure 11 than Figure 12.

The DIC images did not indicate an area of low strain in the suspected notch location, as expected. Following the experiments, it was determined that the notch was not located in the area it was expected.

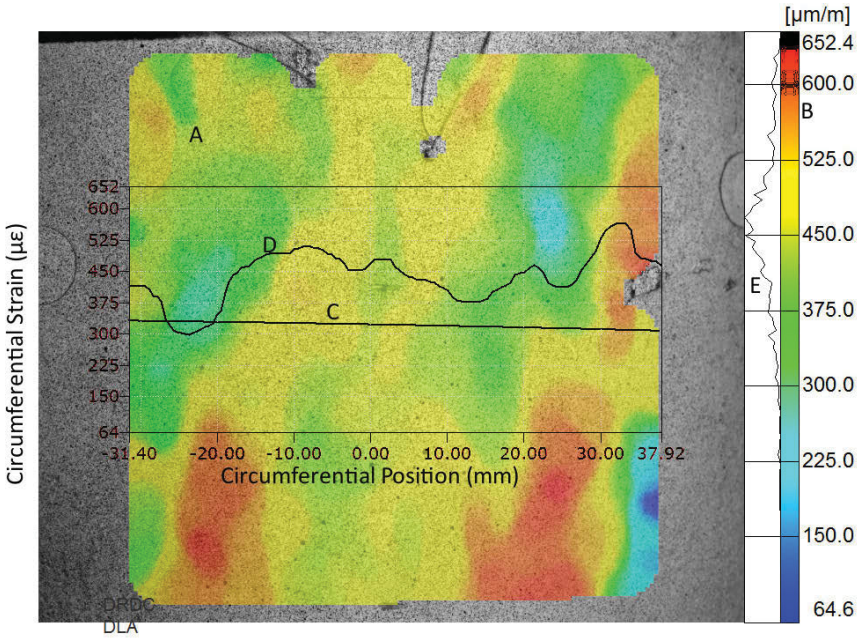

Figure 11: *Sample 1 DIC strain measurements with 19 MPa internal pressure. Notch was supposed to be oriented vertically at the center of the image. Image was taken 30 seconds before that in Figure 12 while the experimental conditions were the same.*

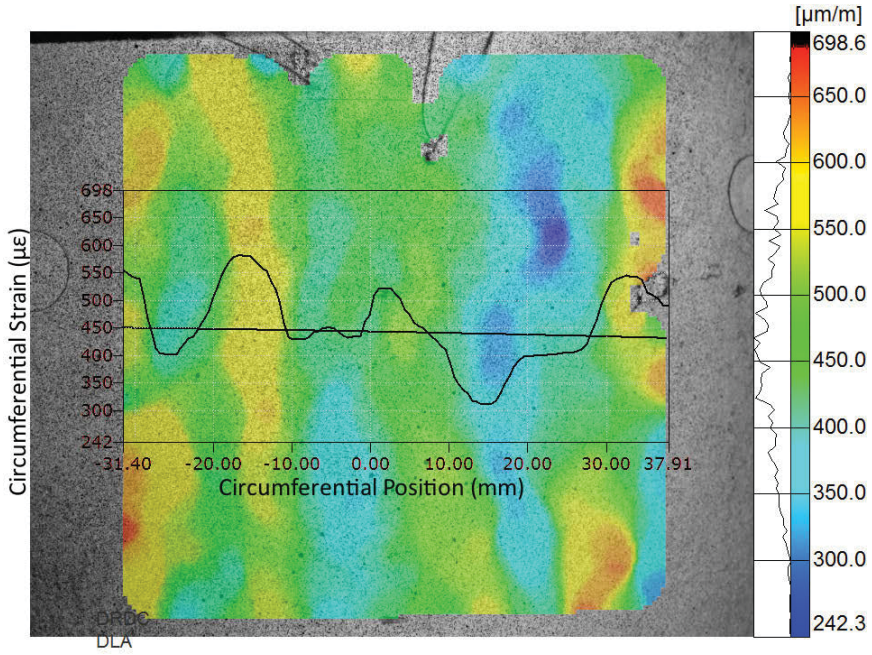

Figure 12: *Sample 1 DIC strain measurements with 19 MPa internal pressure. Notch was supposed to be oriented vertically at the center of the image. Image was taken 30 seconds after that in Figure 11 while the experimental conditions were the same.*

There was a noticeable amount of variation in strain between the consecutive images in Figures 11 and 12 taken 30 seconds apart. The internal pressure was constant between these images. These types of variations were observed in all of the experiments, so they are believed to be experimental noise. Experimental noise is unavoidable, but it is not clear what proportions of the noise were inherent to the technique and which might be reduced by optimizing DIC equipment operation or improving the experimental setup by reducing external vibrations. One speculated source of noise was vibration due to the pump operation.

4.1.2 Locating notch with digital image correlation

Afterwards, the notch locations were approximated visually through the threaded holes at the top of each cylinder and a second experiment was run using DIC equipment only to measure strain in order to more precisely determine the notch location. The experimental samples were pressurized to 20 MPa and DIC measurements were taken. Results from the experiment with Sample 2 are shown in Figures 13 and 14. The vertical blue shape outlines an area of low strain consistent with where the notch was located visually. The shape is similar in the two figures. The histograms indicate the average strain in the images was approximately 450 – 500 $\mu\epsilon$ but there was significantly more variation in Figure 14.

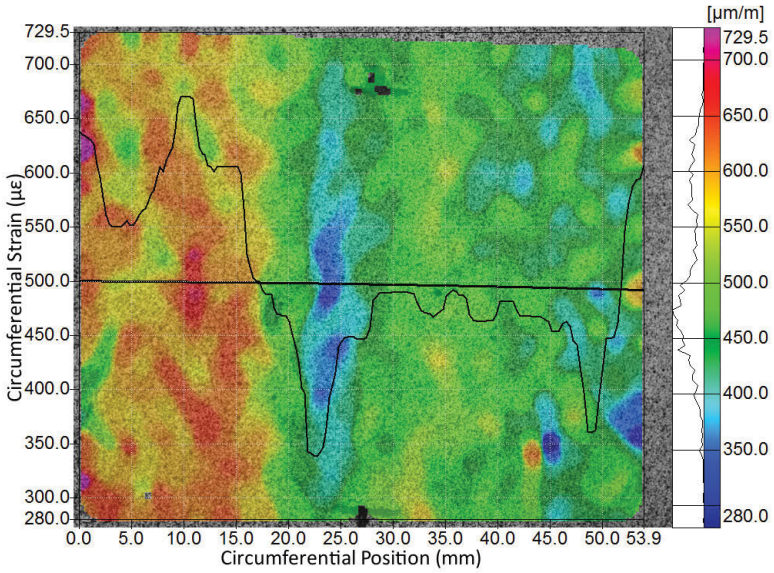

Figure 13: *DIC strain measurements of Sample 2 under 20 MPa internal pressure. Image was taken 30 seconds before that in Figure 14 while the experimental conditions were the same.*

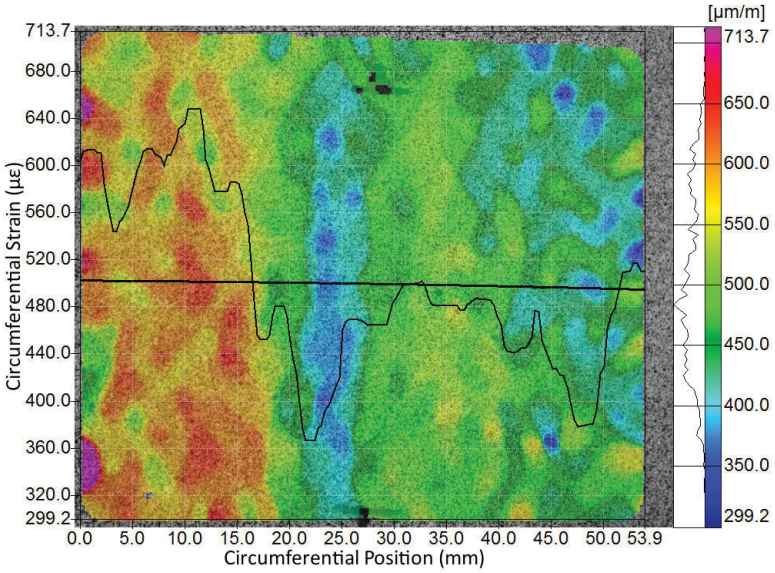

Figure 14: *DIC strain measurements of Sample 2 under 20 MPa internal pressure. Image was taken 30 seconds after that in Figure 13 while the experimental conditions were the same.*

4.1.3 Experiments with corrected notch locations

After the notches had been located more precisely, experiments were run without a speckle pattern on the area where strain gauges were to be applied. This was done to prevent erroneous measurements around the strain gauges and associated wires. Strain gauges were applied prior to pressurizing at the center of the notch, 15 mm on either side circumferentially of the notch, and 90° from the notch.

Sample 2 was pressurized to approximately 25 MPa and DIC images were taken, as shown in Figures 15 and 16. Strain gauge data was not saved due to an error during the experiment, so the data was limited to DIC images taken in the area of the notch. These images turned out quite well: there are few areas of high local strain variation, few blank pixels, and the low strain measurements at the center of the notch and high measurements about 10 mm away are well defined.

Afterwards, each of the specimens was pressurized to 20 MPa and DIC and strain gauge measurements were taken. Images for Sample 1 are shown in Figures 17 and 18. The field of view was enlarged for Sample 2 to determine if the DIC equipment could measure the strain accurately beyond the area of influence of the notch. DIC images from these experiments are shown in Figures 19 and 20.

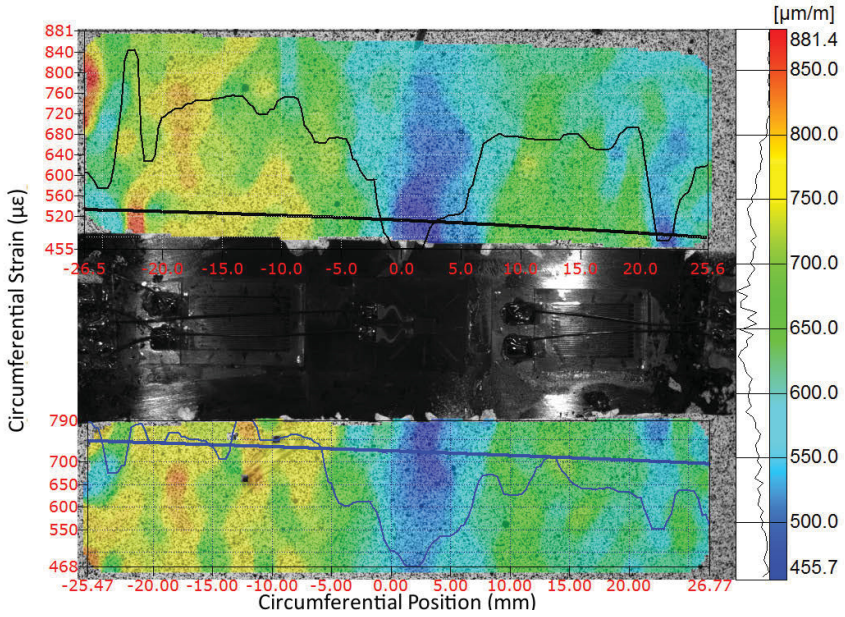

Figure 15: *DIC strain measurements of Sample 2 under ∼25 MPa internal pressure with unpainted strain gauges. Image was taken 30 seconds before that in Figure 16 while the experimental conditions were the same.*

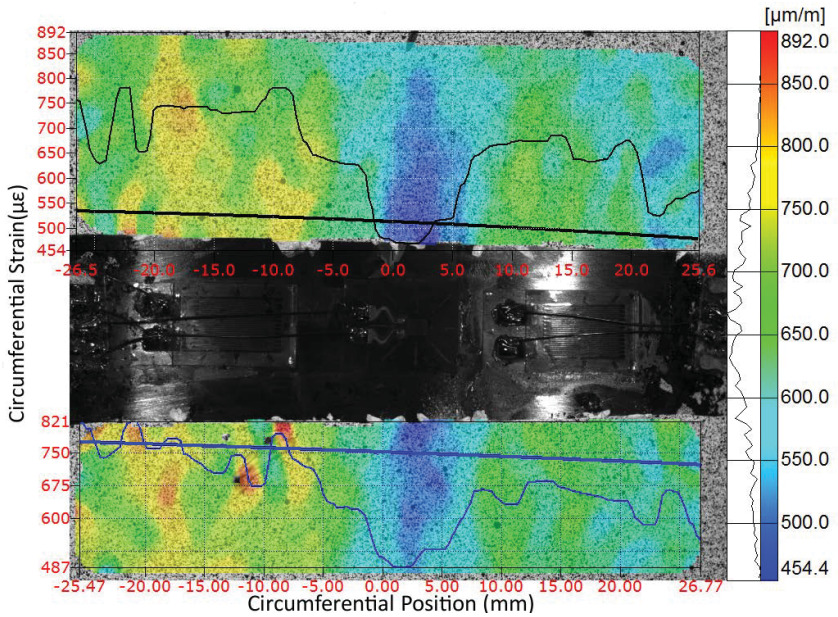

Figure 16: *DIC strain measurements of Sample 2 under ∼25 MPa internal pressure with unpainted strain gauges. Image was taken 30 seconds after that in Figure 15 while the experimental conditions were the same.*

The images from Sample 1 clearly show low strains in the area of the notch and high strains about 10 mm away from the notch. However, local areas of high and low strain are shown where they would not be expected, particularly near the interface of the painted and unpainted regions. These are believed to be experimental artifacts. There were also a number of blank pixels that may have been related to the quality of the speckle pattern as they were reasonably consistent between images. The strain measurements along the virtual strain gauges above and below the strain gauges were similar. Both showed strain values under 400 $\mu\epsilon$ under the notch and between 550 and 600 $\mu\epsilon$ about 10 mm from the notch.

The images from Sample 2 (Figures 19 and 20) do not show the low strains near the center of the notch as clearly as during other experiments, particularly the experiments on the same sample with a smaller field of view and higher internal pressure (Figures 15 and 16). The experimental artifacts near the edge of the field of view, particularly those on the right near the strain gauge wires, showed extreme areas of local strain which reduced the colour contrast in the rest of the image. The virtual strain gauges provide reasonable values near the center of the notch, showing strains of approximately 400 $\mu\epsilon$ at the center of the notch and values of approximately 600 $\mu\epsilon$ about 10 mm from the center. Values along the virtual strain gauges further than 20 mm from the center of the notch appear to be compromised by the artifacts on each side.

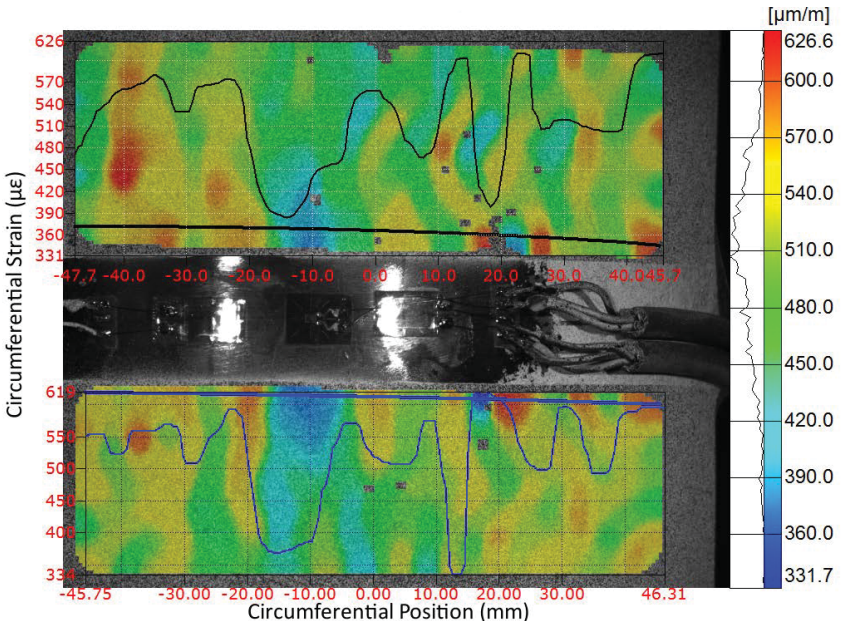

Figure 17: *Digital image correlation measurements of Sample 1 circumferential strain while under 20 MPa internal pressure. Image was taken 30 seconds before that in Figure 18 while the experimental conditions were the same.*

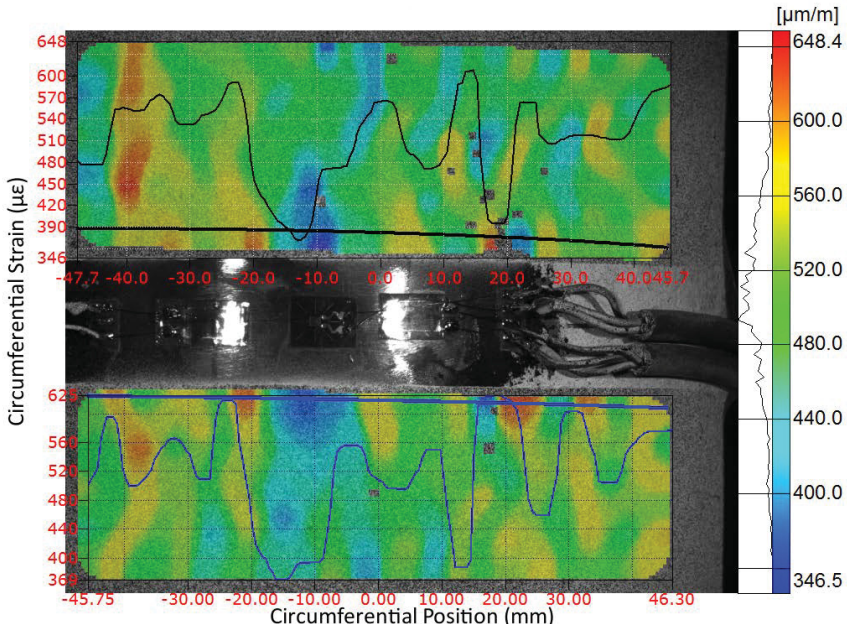

Figure 18: *Digital image correlation measurements of Sample 1 circumferential strain while under 20 MPa internal pressure. Image was taken 30 seconds after that in Figure 17 while the experimental conditions were the same.*

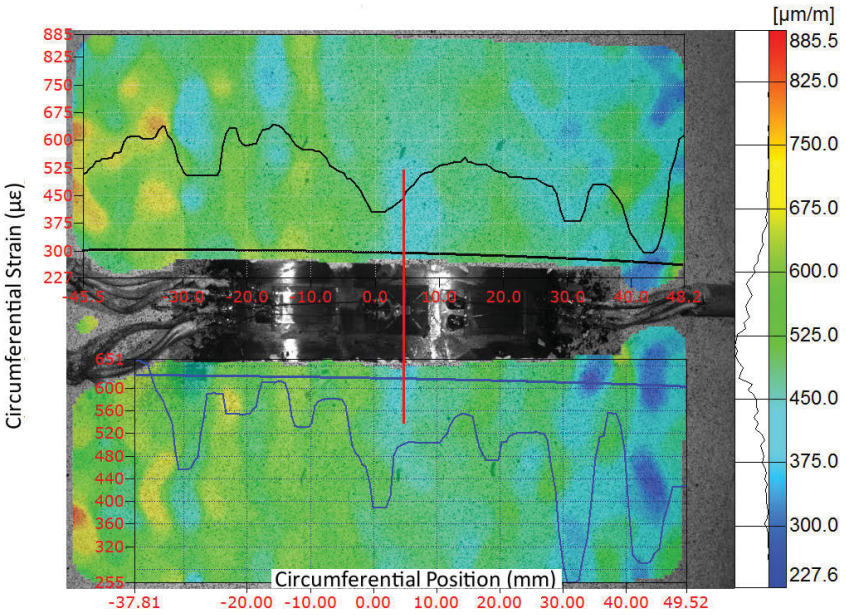

Figure 19: *Digital image correlation measurements of Sample 2 circumferential strain while under 20 MPa internal pressure. Image was taken 30 seconds before that in Figure 20 while the experimental conditions were the same. The red line is the approximate notch location.*

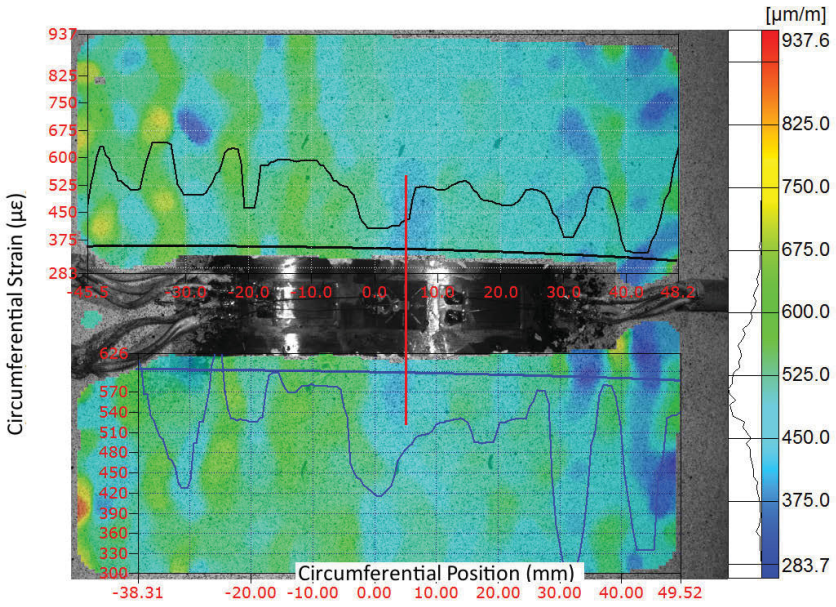

Figure 20: *Digital image correlation measurements of Sample 2 circumferential strain while under 20 MPa internal pressure. Image was taken 30 seconds after that in Figure 19 while the experimental conditions were the same. The red line is the approximate notch location.*

4.2 Finite element analysis results

The deformed shape of the benchmark FE model under a 20 MPa internal pressure load is shown in Figure 21. The response is characterized by a global expansion of the pipe diameter and an outward bending of the end cap. Prying forces due to the pressure load cause the interface between the pipe and end cap to open up. That leads to high stresses near the root of the fillet weld (see Figure 22). It is unlikely that those yield-level stresses would be as severe in practice, since the weld would penetrate further in to the pipe wall. Furthermore, the high stresses are concentrated near the weld and are isolated from the region of interest near the notch. There is also a small area of stresses near the assumed yield strength close to the end of the notch (see Figure 23). That would be important if the aim of the analysis was to predict stress concentration factors for crack growth; however, the goal of the current work is to predict the strains on the outside of the pipe wall, well away from the highest stresses. Thus, it was concluded that the linear-elastic analysis has sufficiently captured the structural response and that a nonlinear-plastic analysis was not justified. The results presented below are for the benchmark model unless otherwise specified.

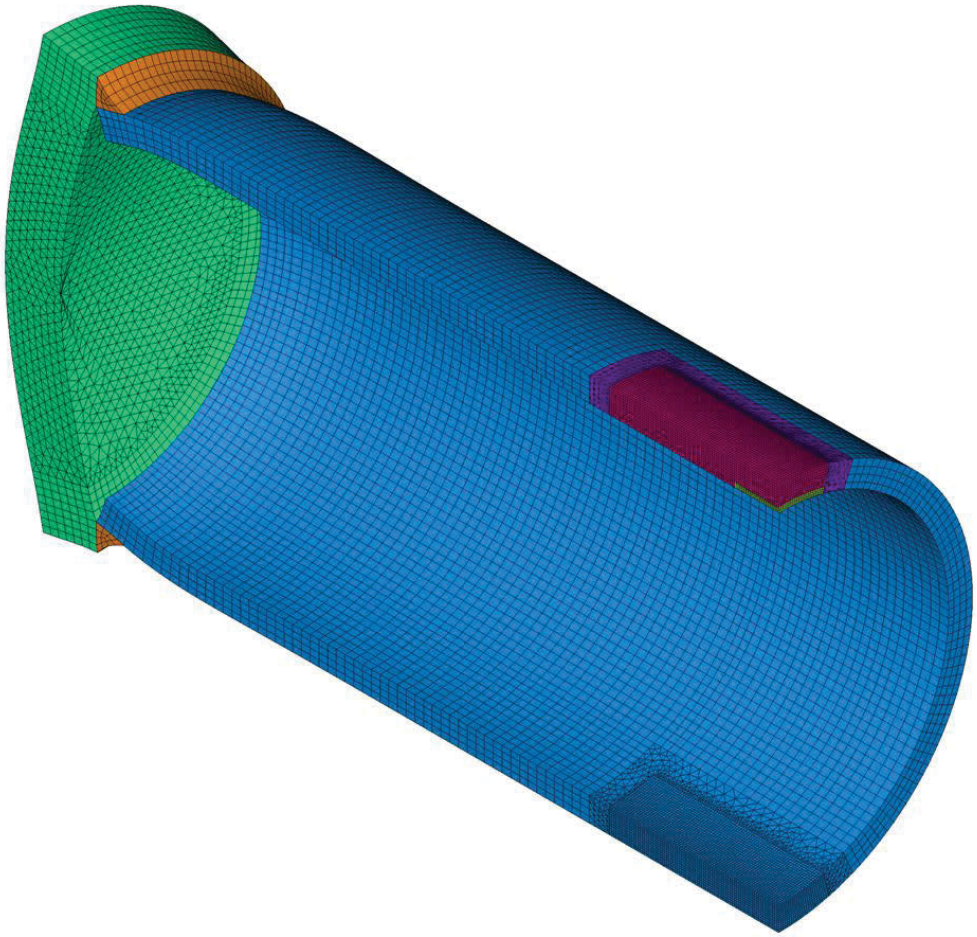

Figure 21: *Deformed finite element mesh under 20 MPa internal pressure load (displacements have been magnified by a factor of 100 for clarity).*

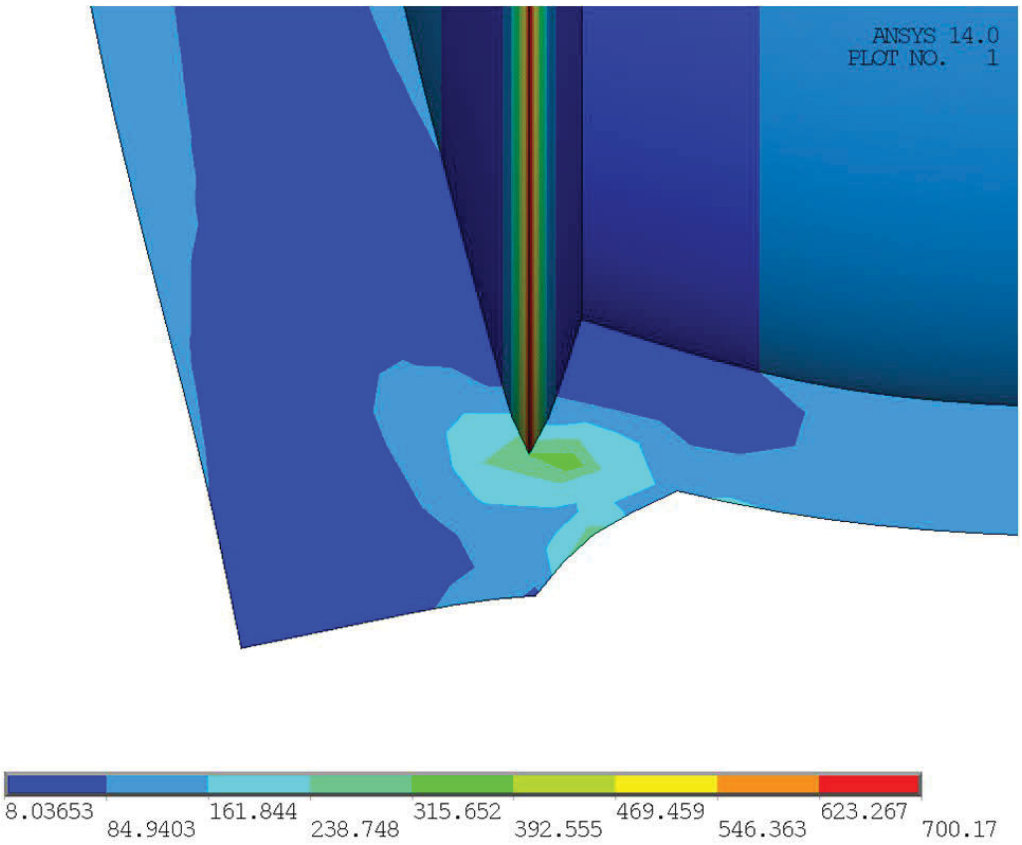

Figure 22: *Contour plot showing the von Mises stress (MPa) in the region of the fillet weld.*

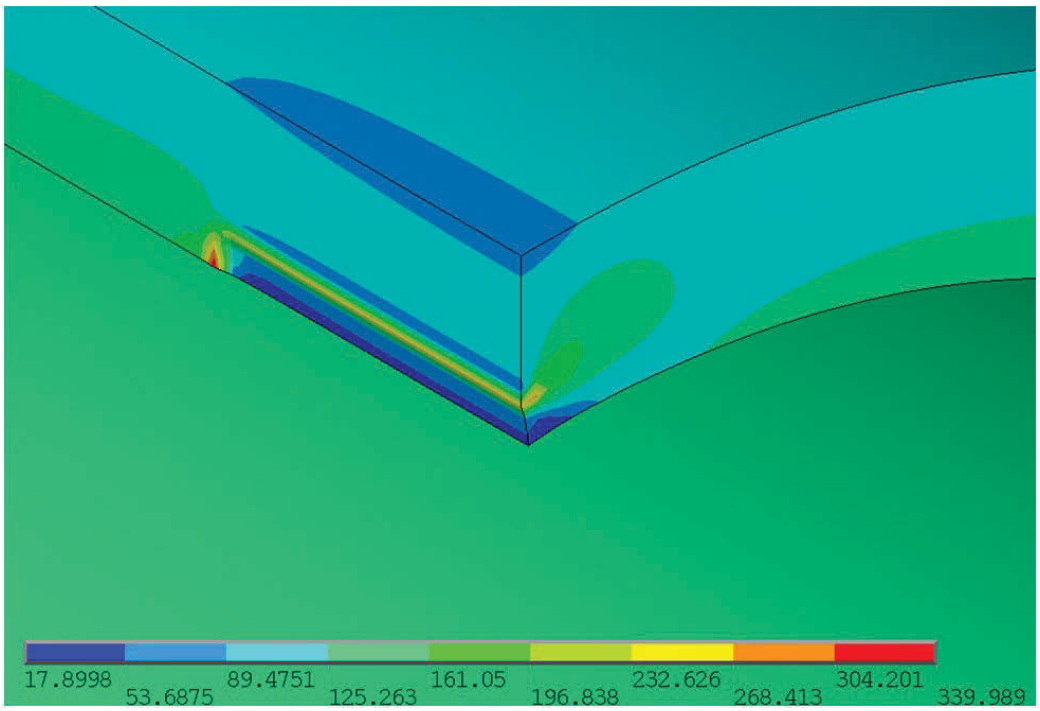

Figure 23: *Contour plot showing the von Mises stress (MPa) in the region of the notch.*

A contour plot of the radial displacements of the FE model is shown in Figure 24. It can be seen that the outward bulging of the pipe is somewhat reduced in the vicinity of the notch. That is because the pipe expansion is partially counteracted in that region by inward bending resulting from the circumferential load-path eccentricity at the notch, which tends to open the notch. The contour plot of the circumferential displacements in Figure 25 shows that the notch opens approximately 0.005 mm under the 20 MPa load.

The hoop strain in the FE model is shown in the contour plot in Figure 26. The hoop strain in the pipe is within 380 and 635 $\mu\epsilon$, except near the fillet weld and the notch. The hoop strain is greatest near the longitudinal and radial tips of the notch (see Figure 27); however, the strain gradients in that area are quite large as well, so that the strain levels are quickly attenuated in the adjacent intact pipe.

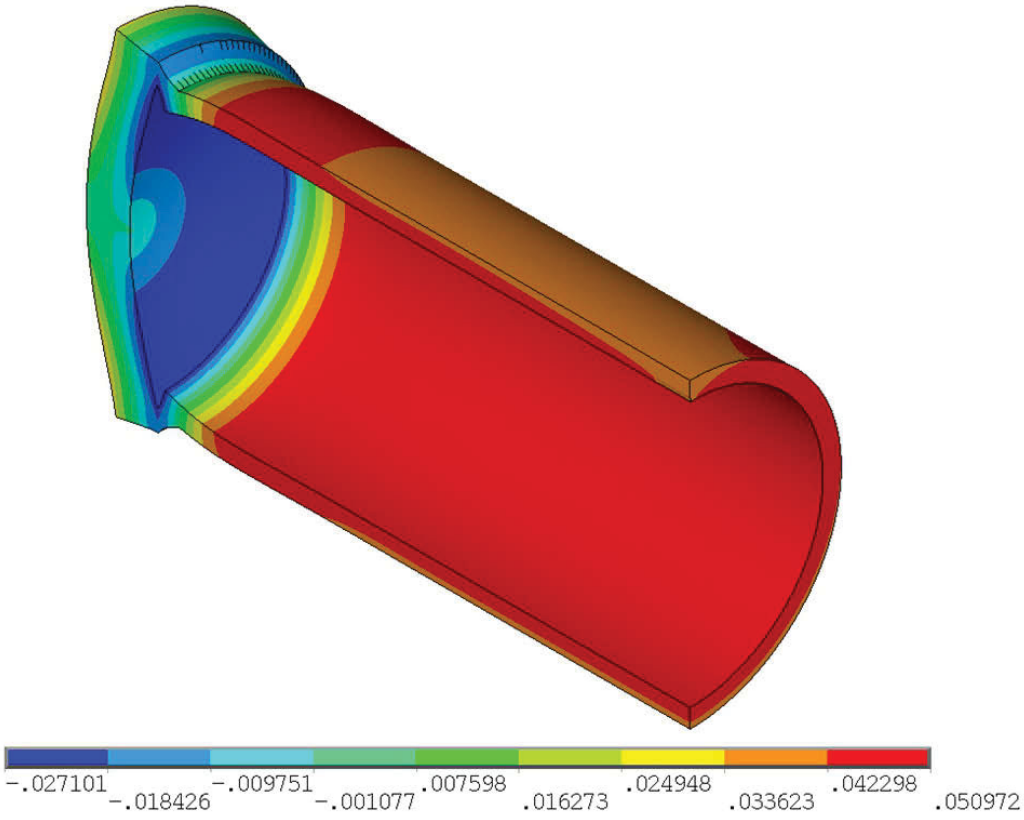

Figure 24: *Contour plot showing the radial displacement (mm) of the test specimen under the 20 MPa internal pressure load. Contours are superimposed on the deformed FE model whereby the displacements have been exaggerated by a factor of 100 for clarity.*

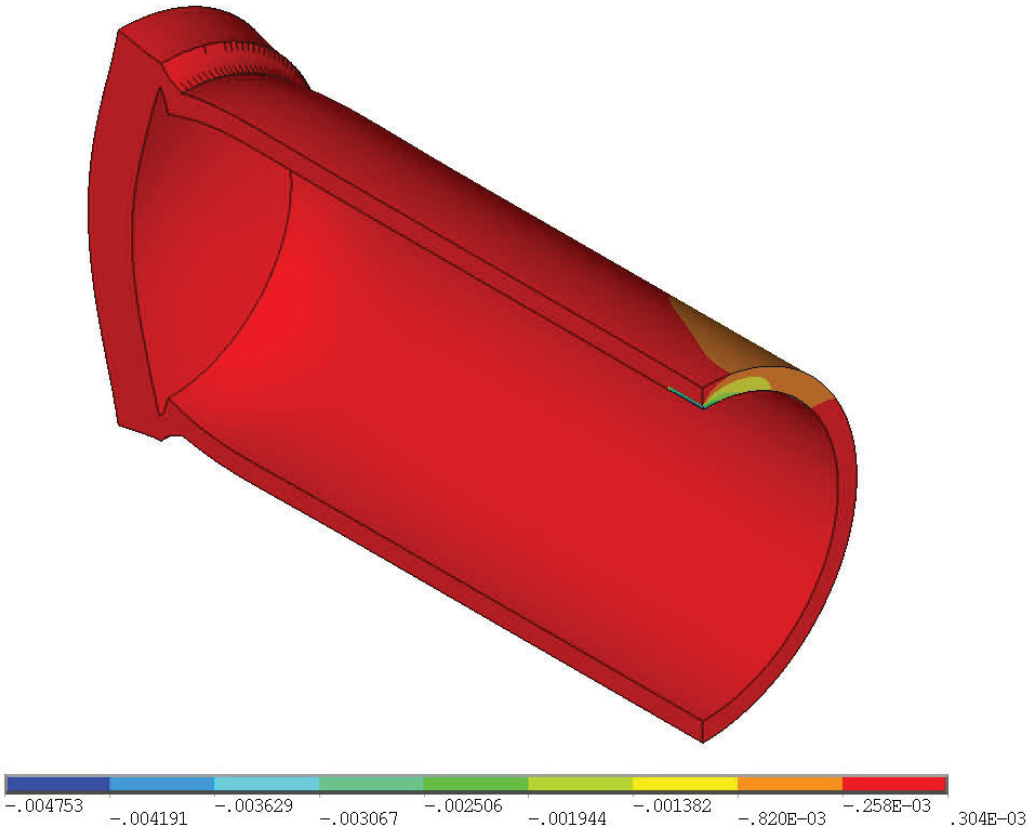

Figure 25: *Contour plot showing the circumferential displacement (mm) of the test specimen under the 20 MPa internal pressure load.*

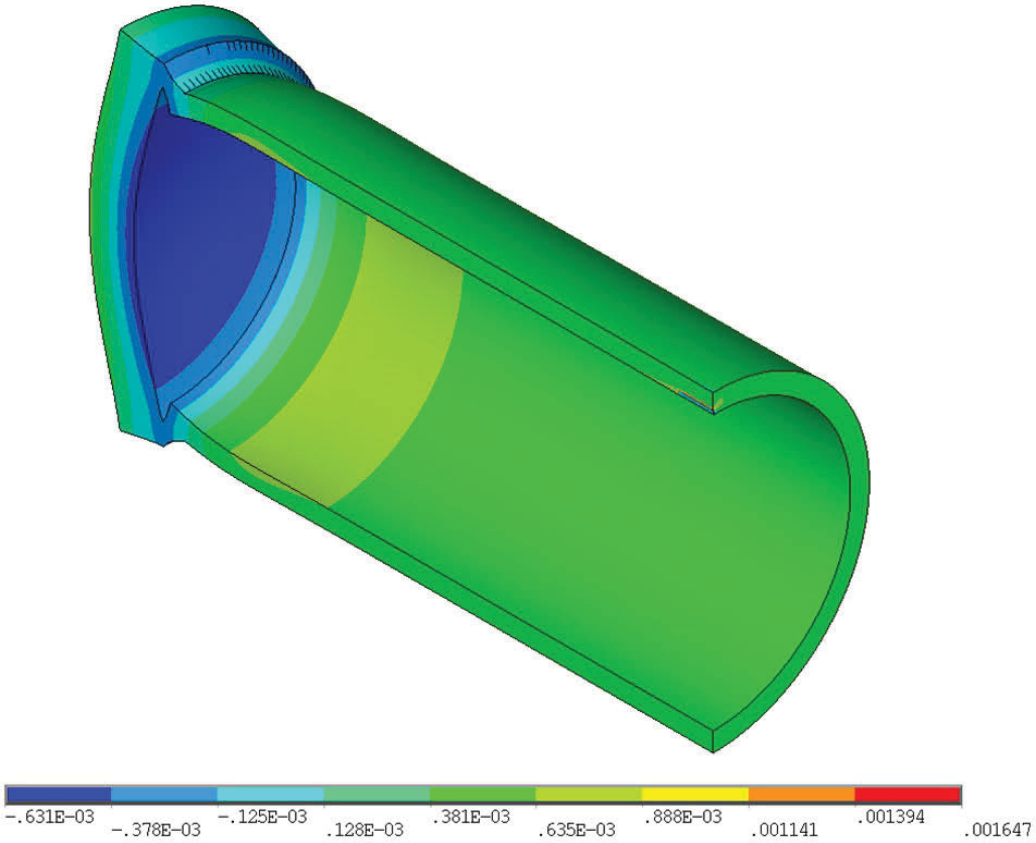

Figure 26: *Contour plot showing the circumferential strain of the test specimen under the 20 MPa internal pressure load.*

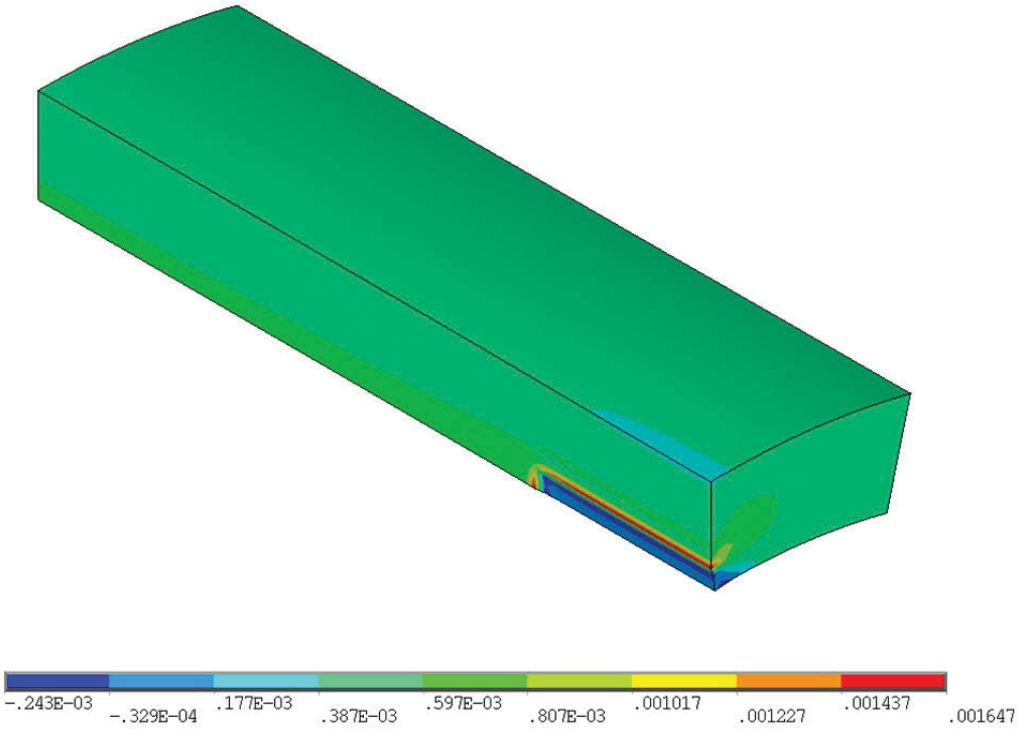

Figure 27: *Contour plot showing the circumferential strain of the notched region of the test specimen under a 20 MPa internal pressure load.*

In Figure 28, the predicted hoop strain on the outside of the pipe wall at mid-length is plotted against the circumferential location. The deep trough in the strain profile at zero degrees corresponds with the notch location and is a result of inward bending associated with opening of the notch. The strain gradient is large, even on the outside of the pipe away from the notch, with the hoop strains increasing from a minimum of 356 $\mu\epsilon$ to a maximum of 542 $\mu\epsilon$ within 12 mm of the notch. The strain level drops off further away from the notch, eventually reaching a stable value of 498±2 $\mu\epsilon$ over approximately 280° of the pipe wall.

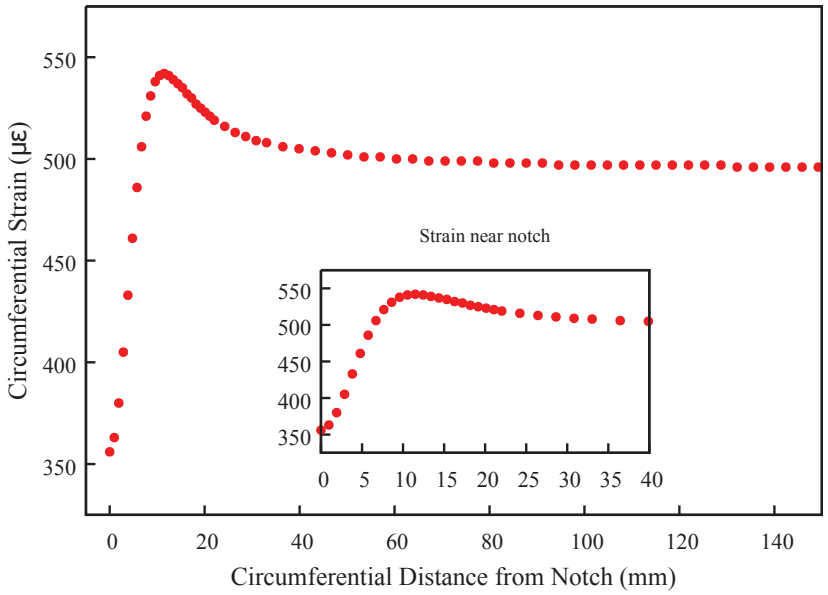

Figure 28: *Circumferential distribution of hoop strain on external pipe wall at mid-length. The 0 mm location corresponds with the location of the 2.5 mm deep notch. Inset shows strain response in vicinity of a notch.*

The hoop strain distributions predicted by the benchmark and refined models are compared in Figure 29. The overall prediction of strain distribution and magnitude did not change when the mesh was refined. With the refined model, the minimum and maximum hoop strains were 354 $\mu\epsilon$ and 543 $\mu\epsilon$, respectively. Those values are within 1% of the values predicted by the benchmark model. Thus, it is concluded that the original benchmark mesh is sufficiently refined since the use of a finer mesh would not lead to significantly different results.

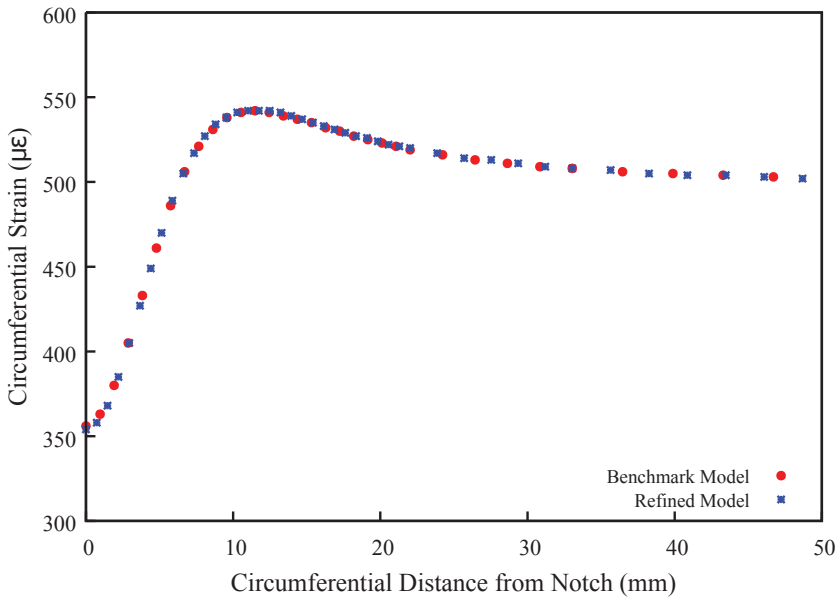

Figure 29: *Circumferential distribution of external surface hoop strain at mid-length showing the strain behaviour predicted by the benchmark (coarser mesh) and refined FE models as a function of the distance from the 2.5 mm deep notch.*

The hoop strain results for the notch depth study are shown in Figure 30. It can be seen that the hoop strain on the external surface of the pipe, directly opposite the notch, decreases as the depth of the notch increases. On the other hand, the maximum hoop strain, which occurs approximately 10 mm away from the notch in the circumferential direction, tends to increase with increasing notch depth. Those trends are attributed to the increase in the load-path eccentricity, and hence the resultant bending moment, as the notch depth increases.

The predicted hoop strain response as a function of crack depth, for various potential strain gauge locations, is shown in Figure 31. That figure shows that, if the strain gauge is well-aligned with the crack location (i.e., at 0 mm), the gauge response will be very sensitive to changes in the crack depth; however, if the gauge location is in error by only 5 mm, the strain response will be approximately static with crack growth. The strain gauge response improves somewhat if the gauge position is even further away from the crack, due to the peak in the strain response in Figure 30, but the best gauge position is clearly directly opposite the crack.

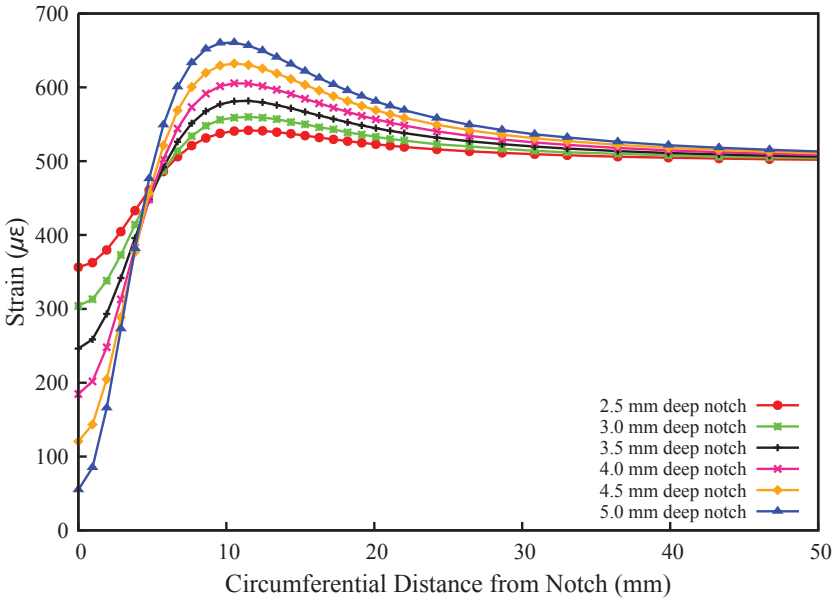

Figure 30: *Circumferential distribution of hoop strain outside the pipe wall at mid-length for a range of crack depths.*

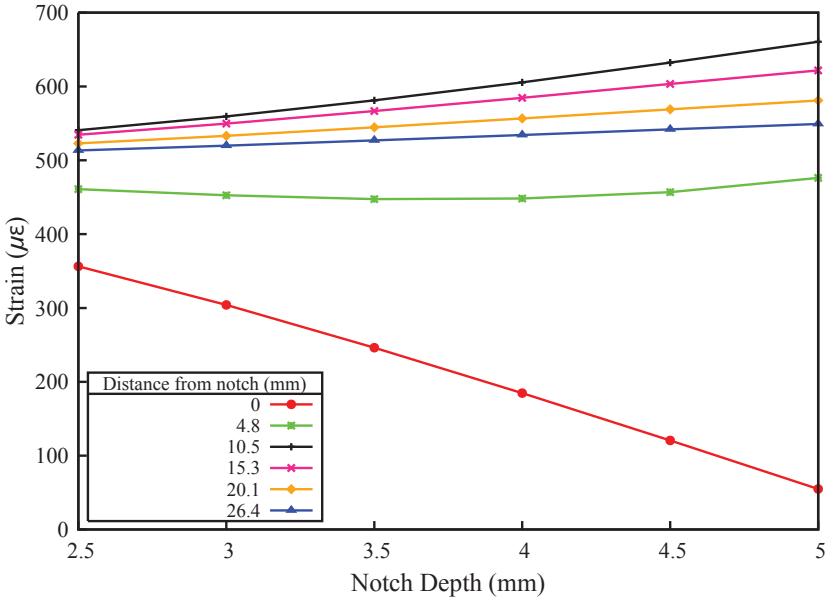

Figure 31: *Relationship between the hoop strain outside the pipe wall at mid-length and the depth of the notch; showing the strain behaviour at several positions relative to the notch location.*

4.3 Comparisons between experimental and FE results

4.3.1 Initial experiment

After the initial experiment, it was determined that the notch was not in the expected location. The strain gauge measurements in the area the notch was expected showed asymmetry in the strain with a minimum 10 mm circumferentially away from the expected center. This is consistent with an incorrect notch location, as the minimum was expected at the center of the notch. The strain gauges 90° from the expected notch yielded measurements of 450 $\mu\epsilon$ and 453 $\mu\epsilon$. These are similar to the FE value scaled to account for the difference in pressure loading, 471 $\mu\epsilon$. There was a significant amount of variation in the DIC strain readings, both within images (particularly in Figure 12) and between images.

4.3.2 Experiment to locate notch

Figures 13 and 14 show the strain field of Sample 2 measured using DIC while it was pressurized to 20 MPa. The images show higher levels of strain 10 – 15 mm to the left of the notch location. This is consistent with the higher strains calculated in the FE model (Figure 28), but the maximum DIC strain measurements in this location are approximately 600 – 650 $\mu\epsilon$, while the FE results were approximately 530 – 540 $\mu\epsilon$. However, the strains on the right side of Figures 13 and 14 are approximately 450 $\mu\epsilon$. This is closer to the value calculated in the FE model 90° from the notch (496 $\mu\epsilon$) than the value calculated for 10 mm circumferentially from the notch (539 $\mu\epsilon$).

4.3.3 Experiments with corrected notch locations

The DIC results from pressurizing Sample 2 to 25 MPa are shown in Figures 15 and 16. The values calculated along the continuous virtual strain gauges above and below the foil strain gauges are compared with the FE calculations scaled to 25 MPa in Table 2. The DIC results are in good agreement with the FE results at the center of the notch and on the right side of the notch. However, on the left side of the notch, the strains measured using DIC are approximately 10 – 20% higher than the right side and the values calculated in the FE analysis.

The DIC results from the experiments where the two samples were pressurized to 20 MPa are shown in Figures 17 – 20. Point measurements of the continuous DIC virtual strain gauges, foil strain gauge measurements, and FE strain results are compared in Tables 3 and 4 for Samples 1 and 2, respectively. The results are plotted in Figure 32.

Table 2: *Comparison of strains measured with DIC virtual strain gauges above and below foil gauges and strains calculated with FE analysis for Sample 2 pressurized to 25 MPa (Figures 15 and 16).*

Figure	Distance from Notch (mm)	Upper DIC Virtual Strain Gauge ($\mu\epsilon$)	Lower DIC Virtual Strain Gauge ($\mu\epsilon$)	FE Strain Results ($\mu\epsilon$)
15	0	460	470	445
	10–15 (left)	700–750	750–790	669–678
	10–15 (right)	650–680	640–700	669–678
16	0	470	490	445
	10–15 (left)	700–780	750–800	669–678
	10–15 (right)	640–680	650–680	669–678

For Sample 1, the DIC point strain measurements were within 12% of the FE strain values. The strain gauge values were within 14% of the FE strain values, except at the center of the notch. The agreement between the strain gauge values and the DIC point values was not as good; the DIC values were approximately 30% greater at the notch but within 20% of the strain gauge values elsewhere.

For Sample 2, all of the DIC point strain measurements were within 20% of the strain values calculated with the FE analyses and most were within 10%. The strain gauge readings were 6 – 16% higher than the FE strain values. Surprisingly, the greatest disagreement between the strain gauge readings and FE results was 90° away from the notch, where the stress field was expected to be affected only by variations in thickness. Most of the DIC and strain gauge readings agreed within 10%, all were within 17%.

Table 3: *Comparison of strain measured with DIC continuous virtual strain gauges above and below foil gauges, strain gauge measurements, and strain calculated with FE analysis for Sample 1 pressurized to 20 MPa. (Figures 17 and 18)*

Figure	Distance from Notch (mm)	Upper DIC Virtual Strain Gauge ($\mu\epsilon$)	Lower DIC Virtual Strain Gauge ($\mu\epsilon$)	Strain Gauge ($\mu\epsilon$)	FE Strain Results ($\mu\epsilon$)
17	0	380	370	282	356
	15 (left)	570	560	611	536
	15 (right)	490	510	601	536
	132	-	-	503	496
18	0	370	370	282	356
	15 (left)	565	620	611	536
	15 (right)	490	500	601	536
	132	-	-	503	496

Table 4: *Comparison of strain measured with DIC continuous virtual strain gauges above and below foil gauges, strain gauge measurements, and strain calculated with FE analysis for Sample 2 pressurized to 20 MPa. (Figures 19 and 20)*

Figure	Distance from Notch (mm)	Upper DIC Virtual Strain Gauge ($\mu\epsilon$)	Lower DIC Virtual Strain Gauge ($\mu\epsilon$)	Strain Gauge ($\mu\epsilon$)	FE Strain Results ($\mu\epsilon$)
19	0	405	390	380	356
	15 (left)	570	530	617	536
	15 (right)	515	475	568	536
	132	-	-	577	496
20	0	425	420	380	356
	15 (left)	600	580	617	536
	15 (right)	475	495	568	536
	132	-	-	577	496

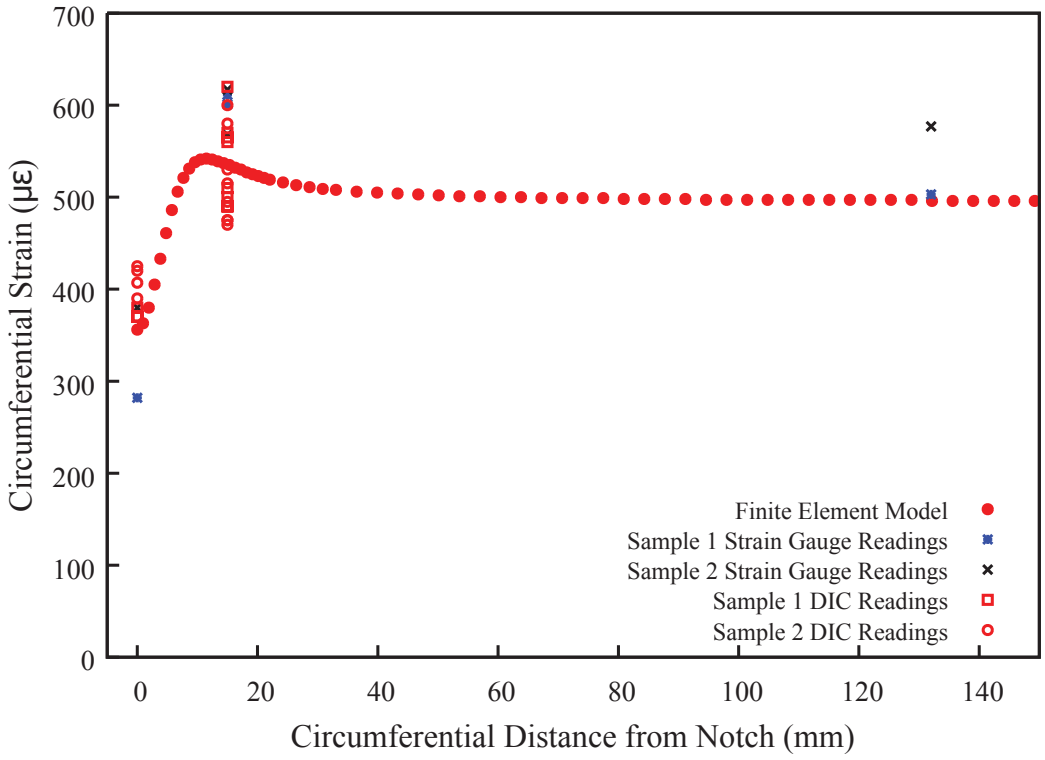

Figure 32: *Strain gauge and DIC strain measurements for experiments with Samples 1 and 2 pressurized to 20 MPa and strains calculated with FE analysis.*

The agreement between the DIC strain readings, strain gauge readings, and strain values calculated with FE analyses is reasonably good. The disagreement and scatter in the data shown in Tables 2 – 4 and Figure 32 are of similar order to the variations in the samples' wall thickness (12.5%).

The reasonable agreement between the external strain calculated in the FE analyses and the strain measured using strain gauges indicates the results from the FE analyses for these cylinders are valid. Since the same method was used to model an HP air bottle, this suggests the FE external strain results for an HP air bottle in the presence of a crack are reliable.

Asymmetry in the strain readings was observed in most of the experiments for both samples. It is not clear what caused this, but one possible source may have been variations in thickness and circularity that were similar in the two samples cut from a single length of pipe.

Digital image correlation proved to be quite useful to precisely locate the notch and measure the strain. However, improvements in the equipment or its operation could yield more reliable results. There were unexpected variations in the strain readings within images and between images taken with identical experimental conditions. The source of these variations was not identified. Improvements in measurements taken near strain gauges, wires, or the interface may result in contour plots that provide useful information more readily.

5 Conclusions

A crack-like indication on a high-pressure air bottle instigated a study to improve the understanding of the effect of an internal crack. Two experimental samples were tested for comparison with an FE model to validate the use of externally mounted strain gauges to monitor further growth of cracks of a limited size. Reasonable agreement of externally mounted strain gauge readings and digital image correlation strain fields with FE analyses suggests the finite element modelling technique used yields reliable results.

Digital image correlation provides a means to measure the strain field of a loaded material. In this study, it proved to be quite useful to precisely locate an internal notch due to a 28% reduction in strain opposite the notch center. This technology could be useful to locate internal cracks in HP air bottles due to strain reduction opposite the crack center; a reduction of 26% was calculated with a 2 mm deep, 10 mm long crack. DIC could also be used to verify the presence of a crack after detection of crack-like indications using other non-destructive examination techniques. Although it can precisely determine the location of a crack, coupling with finite element analysis to compare the strain field may be necessary to determine the flaw size. As DIC has not been used as much as traditional non-destructive examination techniques, it is not as easy to use or as reliable. However, it provides a useful complement to existing non-destructive examination techniques.

Further development is required before DIC should be used more extensively in service. Future work to reduce experimental artifacts at the edge of the field of view and in the area of strain gauge wires would make images easier to interpret. Optimization of DIC equipment operation could result in improvements to the field of view, precision of results, as well as reduction and quantification of noise within and between images.

The results of the air bottle crack modelling analyses indicated that the external strain will be influenced by the presence of an internal crack. A 2 mm deep, 10 mm long crack would cause a decrease in external strain of 304 $\mu\epsilon$ immediately opposite a crack in a bottle that would otherwise have an external strain of 1192 $\mu\epsilon$. The strain at locations 8 mm away from a crack circumferentially would be higher than in the absence of a crack. The differences in strain at both locations will increase as a crack grows. The differences in external strain are sufficient to be measured by externally-mounted foil strain gauges, but it is necessary for the gauges to be located precisely. The application of strips of strain gauges should provide a means of ensuring the locations exhibiting changing strain can be monitored.

This work shows that externally mounted strain gauges provide a feasible method to monitor existing cracks in cases where it is necessary for a naval platform to operate with a cracked HP air bottle. If this monitoring is conducted, the finite element methodology described in this report can be used to predict strain readings for the detected crack and growing cracks.

References

[1] Lyczko, S. (2006), Evaluation of HMCS VICTORIA High Pressure Cylinders, (Technical Report 2711 (NETE SL) IT2113-R) NETE.

[2] Braun, D. (2010), High-Pressure Air Bottle Fatigue Analysis, (Technical Report DRDC Atlantic CR 2010-031) BMT Fleet Technology.

[3] (2000), Defence Standard 02-317, Requirements for Non-Transportable Pressure Vessels for the Storage of High Pressure Gases, Part 2, Manufacture, Inspection & Testing, United Kingdom Ministry of Defence.

[4] (2010), Defence Standard 02-318, Non-Transportable High Pressure Gas Cylinders Periodic Inspection, Testing and Maintenance, Part 1, Onboard Shop Testing of High Pressure Gas Cylinders, United Kingdom Ministry of Defence.

[5] (2010), Defence Standard 02-318, Non-Transportable High Pressure Gas Cylinders Periodic Inspection, Testing and Maintenance, Part 2, In-Situ On-Board Testing of High Pressure Gas Cylinders, United Kingdom Ministry of Defence.

[6] Hudak, Jr., S. J., Hanley, J. J., Lukezich, S. J., Connolly, M. P., Nilsen, L. N., and Nguyen, S. (1997), A Damage Tolerance Approach for Recertification of High-Pressure Flasks, *Association of Scientist and Engineers 34th Annual Technical Symposium*.

[7] Laplante, D., Lyczko, S., and Sankey, D. (Summer 2006), Recertifying Submarine High-Pressure Cylinders in situ, *Maritime Engineering Journal*, pp. 26 – 28.

[8] (2012), Personal communication between I. Thompson, DRDC Atlantic, and S. Lyczko, NETE.

[9] Thompson, I. (2010), High-Pressure Air Bottle Crack Propagation Study, (Technical Report 3771-2-1.46) DRDC Atlantic.

[10] Bruck, H., McNeill, S., Sutton, M., and Peters, III, W. (1989), Digital Image Correlation Using Newton-Raphson Method of Partial Differential Correction, *Experimental Mechanics*, 29(3), 261–267.

List of Symbols/Acronyms

2c	crack length
a	crack depth
DIC	digital image correlation
FE	finite element
HP	high-pressure
NETE	Naval Engineering Test Establishment

This page intentionally left blank.

DOCUMENT CONTROL DATA

(Security markings for the title, abstract and indexing annotation must be entered when the document is Classified or Designated.)

1. ORIGINATOR (The name and address of the organization preparing the document. Organizations for whom the document was prepared, e.g. Centre sponsoring a contractor's report, or tasking agency, are entered in section 8.)

DRDC – Atlantic Research Centre
PO Box 1012, Dartmouth NS B2Y 3Z7, Canada

2a. SECURITY MARKING (Overall security marking of the document, including supplemental markings if applicable.)

UNCLASSIFIED

2b. CONTROLLED GOODS

(NON-CONTROLLED GOODS)
DMC A
REVIEW: GCEC APRIL 2011

3. TITLE (The complete document title as indicated on the title page. Its classification should be indicated by the appropriate abbreviation (S, C or U) in parentheses after the title.)

Validation of new crack monitoring technique for Victoria class high-pressure air bottles

4. AUTHORS (Last name, followed by initials – ranks, titles, etc. not to be used.)

Thompson, I.; MacKay, J. R.

5. DATE OF PUBLICATION (Month and year of publication of document.)	6a. NO. OF PAGES (Total containing information. Include Annexes, Appendices, etc.)	6b. NO. OF REFS (Total cited in document.)
June 2014	56	10

7. DESCRIPTIVE NOTES (The category of the document, e.g. technical report, technical note or memorandum. If appropriate, enter the type of report, e.g. interim, progress, summary, annual or final. Give the inclusive dates when a specific reporting period is covered.)

Scientific Report

8. SPONSORING ACTIVITY (The name of the department project office or laboratory sponsoring the research and development – include address.)

DRDC – Atlantic Research Centre
PO Box 1012, Dartmouth NS B2Y 3Z7, Canada

9a. PROJECT OR GRANT NO. (If appropriate, the applicable research and development project or grant number under which the document was written. Please specify whether project or grant.)	9b. CONTRACT NO. (If appropriate, the applicable number under which the document was written.)
11ga07	

10a. ORIGINATOR'S DOCUMENT NUMBER (The official document number by which the document is identified by the originating activity. This number must be unique to this document.)	10b. OTHER DOCUMENT NO(s). (Any other numbers which may be assigned this document either by the originator or by the sponsor.)
DRDC-RDDC-2014-R81	

11. DOCUMENT AVAILABILITY (Any limitations on further dissemination of the document, other than those imposed by security classification.)

(X) Unlimited distribution
( ) Defence departments and defence contractors; further distribution only as approved
( ) Defence departments and Canadian defence contractors; further distribution only as approved
( ) Government departments and agencies; further distribution only as approved
( ) Defence departments; further distribution only as approved
( ) Other (please specify):

12. DOCUMENT ANNOUNCEMENT (Any limitation to the bibliographic announcement of this document. This will normally correspond to the Document Availability (11). However, where further distribution (beyond the audience specified in (11)) is possible, a wider announcement audience may be selected.)

Unrestricted

13. ABSTRACT (A brief and factual summary of the document. It may also appear elsewhere in the body of the document itself. It is highly desirable that the abstract of classified documents be unclassified. Each paragraph of the abstract shall begin with an indication of the security classification of the information in the paragraph (unless the document itself is unclassified) represented as (S), (C), or (U). It is not necessary to include here abstracts in both official languages unless the text is bilingual.)

High-pressure air bottles are used in the Victoria class submarines to supply breathing air and to provide pressurized air for surfacing. The bottles are exposed to cyclic loading, which may result in the initiation and growth of fatigue cracks. An internal crack-like indication in a high-pressure air bottle instigated this study to better understand the growth of potential fatigue cracks. This will enable better management of the remaining operating life of high-pressure air bottles with detected cracks.

In this study, the feasibility of using externally-mounted strain gauges to monitor the growth of known internal cracks in high-pressure air bottles was examined. A combination of numerical modelling and experiments was used to validate this technique. Two experimental samples were internally pressurized and external strain was measured. Reasonable agreement of measured strain with finite element analyses of the samples suggests the high-pressure air bottle finite element analyses results are reliable. Finite element analyses and experiments showed an area on the exterior of test samples opposite an internal notch with a modified strain field. The numerical analyses indicated that changes in the strain field associated with crack growth may be detected using external strain gauges. These results are consistent with a previous numerical analysis of a high-pressure air bottle which indicated the growth of internal cracks can be monitored with external strain gauges.

Digital image correlation was used to measure the strain field in the area opposite the internal notch. It was useful for identifying the precise location of the notch, but further improvements to its use are necessary to ensure reliable results. It shows promise as a method to identify the location of high-pressure air bottle internal cracks and to complement other non-destructive examination techniques.

14. KEYWORDS, DESCRIPTORS or IDENTIFIERS (Technically meaningful terms or short phrases that characterize a document and could be helpful in cataloguing the document. They should be selected so that no security classification is required. Identifiers, such as equipment model designation, trade name, military project code name, geographic location may also be included. If possible keywords should be selected from a published thesaurus. e.g. Thesaurus of Engineering and Scientific Terms (TEST) and that thesaurus identified. If it is not possible to select indexing terms which are Unclassified, the classification of each should be indicated as with the title.)

high-pressure air bottles, Victoria class submarine, digital image correlation, crack monitoring, fatigue, finite element

DRDC | RDDC

SCIENCE, TECHNOLOGY AND KNOWLEDGE FOR CANADA'S DEFENCE AND SECURITY | SCIENCE, TECHNOLOGIE ET SAVOIR POUR LA DÉFENSE ET LA SÉCURITÉ DU CANADA

www.drdc-rddc.gc.ca